The Astrophysical Journal, 975:252 (19pp), 2024 November 10 https://doi.org/10.3847/1538-4357/ad807f

Self-similar Buildup and Inside-out Growth: Tracing the Evolution of Intermediate-to-high-mass Star-forming Galaxies since $z = 2$

Maryam Hasheminia[1,2,3], Moein Mosleh[2,3], S. Zahra Hosseini-ShahiSavandi[2,4], and Sandro Tacchella[5,6]
[1] Department of Physics, Institute for Advanced Studies in Basic Sciences (IASBS), 444 Prof. Yousef Sobouti Boulevard, Zanjan 45137-66731, Iran
[2] Biruni Observatory, College of Science, Shiraz University, Shiraz 71946-84795, Iran; moein.mosleh@shirazu.ac.ir
[3] Department of Physics, College of Science, Shiraz University, Shiraz 71946-84795, Iran
[4] Department of Physics and Astronomy, University of Padua, Vicolo Osservatorio 3, 35122 Padova, Italy
[5] Kavli Institute for Cosmology, University of Cambridge, Madingley Road, Cambridge, CB3 0HA, UK
[6] Cavendish Laboratory, University of Cambridge, 19 JJ Thomson Avenue, Cambridge, CB3 0HE, UK
Received 2024 July 18; revised 2024 September 5; accepted 2024 September 25; published 2024 November 7

Abstract

We aim to discern scenarios of structural evolution of intermediate-to-high-mass star-forming galaxies (SFGs) since cosmic noon by comparing their stellar mass profiles with present-day stellar masses of $\log(M_{*,0}/M_{\odot}) = 10.3 - 11$. We addressed discrepancies in the size evolution rates of SFGs, which may be caused by variations in sample selection and methods for size measurements. To check these factors, we traced the evolution of individual galaxies by identifying their progenitors using stellar mass growth histories (SMGHs), integrating along the star-forming main sequence and from the IllustrisTNG simulations. Comparison between the structural parameters estimated from the mass- and light-based profiles shows that mass-weighted size evolves at a slower pace compared to light-based ones, highlighting the need to consider the mass-to-light ratio (M/L) gradients. Additionally, we observed mass-dependent growth in stellar mass profiles: massive galaxies ($\log(M_{*,0}/M_{\odot}) \gtrsim 10.8$) formed central regions at $z \gtrsim 1.5$ and grew faster in outer regions, suggesting inside-out growth, while intermediate-mass and less massive SFGs followed a relatively self-similar mass buildup since $z \sim 2$. Moreover, slopes of observed size evolution conflict with the predictions of TNG50 for samples selected using the same SMGHs across our redshift range. To explore the origin of this deviation, we examined changes in angular momentum (AM) retention fraction using the half-mass size evolution and employing a simple disk formation model. Assuming similar dark matter halo parameters, our calculations indicate that the AM inferred from observations halved in the past 10 Gyr while it remained relatively constant in TNG50. This higher AM in simulations may be due to the accretion of high-AM gases into disks.

Unified Astronomy Thesaurus concepts: Galaxies (573); Galaxy radii (617); Galaxy evolution (594); Galaxy structure (622); Galaxy disks (589); Late-type galaxies (907); Magnetohydrodynamical simulations (1966)

1. Introduction

Despite the notable progress achieved in extragalactic astrophysics, questions persist regarding the construction of galaxies' structural components and the mechanisms involved. It is known that star-forming galaxies (SFGs) assemble their stellar mass through star formation (SF), which is regulated by feedback mechanisms, accretion of gas, and minor mergers. Furthermore, various internal and external processes, such as bar and disk instability and clump migration, can transfer or redistribute the stellar mass (M. Noguchi 1999; G. Kauffmann et al. 2004; J. Kormendy & R. C. Kennicutt 2004; F. Bournaud et al. 2007; R. Genzel et al. 2008; A. Dekel et al. 2009; M. R. Krumholz & A. Dekel 2010). Nevertheless, how these processes operate on distinct regions of galaxies and which ones are more effective across different masses and redshifts are still debated.

Each internal and external mechanism leaves distinctive imprints on the stellar mass distribution within galaxies; consequently, by investigating the assembly history of the stellar mass within galaxies, it becomes possible to impose better constraints on existing galaxy formation and evolution scenarios. Therefore, many studies have explored the stellar mass buildup in SFGs over cosmic time and showed that SFGs in general, and particularly the high-mass ones, accumulate their stellar mass from the central regions outward, namely the inside-out growth (P. G. van Dokkum et al. 2010; D. Szomoru et al. 2011; M. Hilz et al. 2013; S. G. Patel et al. 2013b; P. G. van Dokkum et al. 2015; E. J. Nelson et al. 2016; A. R. Hill et al. 2017; C. Abdurro'uf et al. 2023). The main evidence provided for this model is the notably smaller size of high-redshift galaxies compared to their local counterparts, as well as centrally concentrated stellar mass surface density profiles of galaxies directly derived from their light distribution. In contrast, some observations have indicated a slower evolution in the size of SFGs compared to quiescent galaxies (QGs) at a fixed mass and mainly at redshifts $\lesssim$1.5–2 (M. Barden et al. 2005; I. Trujillo et al. 2006; E. Curtis-Lake et al. 2016; M. Mosleh et al. 2017; E. F. Jiménez-Andrade et al. 2019; K. A. Suess et al. 2019a; M. Mosleh et al. 2020; Z. Ji & M. Giavalisco 2023). In some studies, the little evolution in size is argued to be related to the moderately flat specific SF rate (sSFR) profiles obtained from observations and simulations, hence showing that the assembly of their stellar contents is relatively self-similar (P. G. van Dokkum et al. 2013; S. G. Patel et al. 2013a; C. Liu et al. 2017; W. Wang et al. 2017; S. Tacchella et al. 2018; D. Nelson et al. 2019; K. A. Suess et al. 2019b; E. J. Nelson et al. 2021). The "self-similar growth" scenario suggests that mass builds up

simultaneously across all radii at approximately the same rate through mainly SF activities. These diverse scenarios emphasize the need for more detailed studies on the stellar mass growth history (SMGH) of SFGs to discern the dominant growth pattern in each mass regime and the underlying mechanisms that drive it.

The discrepancy in the interpretation of different scenarios is mainly based on the variation in measurements of the structural parameters such as size and the Sérsic index. This can be exemplified in a wide range of slopes that have been measured in the literature for the size evolution of SFGs as a function of redshift, i.e., $r \propto (1+z)^{\gamma}$, in which γ spans from $\sim$0 to -3. Various studies reported a significant growth in the size of SFGs, with slopes ranging from -1 (R. J. Bouwens et al. 2004; T. Dahlen et al. 2007; R. J. Williams et al. 2010; K.-H. Huang et al. 2013; B. W. Holwerda et al. 2015; C. Papovich et al. 2015; L. Yang et al. 2021) to -1.5 (H. C. Ferguson et al. 2004; N. P. Hathi et al. 2008), or somewhere in between (P. G. van Dokkum et al. 2010; P. A. Oesch et al. 2010; M. Mosleh et al. 2011, 2012; Y. Ono et al. 2013; T. Shibuya et al. 2015; R. Kawamata et al. 2018; L. Lindroos et al. 2018; T. Shibuya et al. 2019). Interestingly, even larger rates are predicted in some simulations and semianalytical models (C. Liu et al. 2017; M. A. Marshall et al. 2019; W. J. Roper et al. 2022). On the other hand, many studies have found that the slope of size evolution can be comparatively shallower, between -0.5 and -0.9 (F. Buitrago et al. 2008; M. Franx et al. 2008; V. A. Bruce et al. 2014; T. Morishita et al. 2014; A. van der Wel et al. 2014; R. J. Allen et al. 2017; A. Paulino-Afonso et al. 2017; L. A. Mowla et al. 2019; C. Gómez-Guijarro et al. 2022; K. Ormerod et al. 2024), or even lower (I. Trujillo et al. 2006; M. Mosleh et al. 2017, 2020; E. F. Jiménez-Andrade et al. 2019; M. Hasheminia et al. 2022; Z. Ji & M. Giavalisco 2023; T. Morishita et al. 2024). Such a discrepancy in the rate of size evolution can be attributed to two primary factors: the approach taken to choose a sample, and the way in which the sizes are measured.

To accurately comprehend the growth of individual galaxies, it is crucial to reconstruct the evolutionary path of each galaxy, which observationally is challenging. Several approaches have been suggested to establish a connection between progenitors and descendants and trace the potential pathway of evolution for each galaxy. The most widely employed approach is reconstructing the mass growth history using number density arguments (P. G. van Dokkum et al. 2010; S. G. Patel et al. 2013b; P. G. van Dokkum et al. 2013; A. Whitney et al. 2019), abundance matching (C. Papovich et al. 2015), and the evolution of the SFR–mass relation (S. G. Patel et al. 2013a; M. Hasheminia et al. 2022; A. George et al. 2024). Using the constant number density method, S. G. Patel et al. (2013b) determined a slope of 0.63 for SFGs with a final mass of $10^{11.2}$ $M_{\odot}$. Similar patterns of slower growth can also be seen in other studies that rely on progenitor selection (S. G. Patel et al. 2013a; P. G. van Dokkum et al. 2013; A. Whitney et al. 2019; M. Hasheminia et al. 2022; Z. Ji & M. Giavalisco 2023; A. George et al. 2024), whereas steeper slopes were reported for samples selected at fixed mass (F. Buitrago et al. 2008; A. van der Wel et al. 2014; R. J. Allen et al. 2017; A. L. Faisst et al. 2017; L. A. Mowla et al. 2019). Over a similar redshift range to that of S. G. Patel et al. (2013b), A. van der Wel et al. (2014) and L. A. Mowla et al. (2019) found mass-dependent slopes of 0.8 and 0.9 for the size evolution of SFGs at the fixed mass bins of $\log(M_{*}/M_{\odot}) = [11-11.5]$ and [10.75–11.3], respectively. The progenitor bias, as evidenced in Z. Ji & M. Giavalisco (2023), is probably responsible for these higher rates.

In addition, the obtained size growth rate is significantly influenced by the observing band, as different wavelengths are more sensitive to distinct stellar populations. UV and shorter optical wavelengths are generally more sensitive to young blue populations, whereas longer optical and near-IR (NIR) wavelengths are suitable for tracing the old red components, leading to variations in structural parameters based on wavelength (R. F. Peletier & M. Balcells 1996; C. Möllenhoff et al. 2006; A. W. Graham & C. C. Worley 2008; F. La Barbera et al. 2010; B. Vulcani et al. 2014; R. Lange et al. 2015; E. F. Jiménez-Andrade et al. 2021). Moreover, dust attenuation and metallicity gradient, often present in early-type galaxies, can affect the galaxy's flux, so its size and shape may be changed in different observing bands (D. Pierini et al. 2004; R. J. Tuffs et al. 2004; C. Möllenhoff et al. 2006; A. W. Graham & C. C. Worley 2008; F. La Barbera et al. 2010; L. S. Kelvin et al. 2012; B. Vulcani et al. 2014; R. Lange et al. 2015). A color gradient is caused by these factors, which result in radial mass-to-light ratios (M/L) in galaxies. Due to the radial variations in M/L, especially in SFGs, the light distribution strongly depends on the observed wavelength and may not coincide with the mass distribution. Previous studies indicate that galaxies, on average, tend to have a negative color gradient, implying that UV/optical radii (hereafter half-light) are often larger than mass-based/NIR ones and decrease with increasing wavelength (D. Szomoru et al. 2013; S. Wuyts et al. 2013; J. C. C. Chan et al. 2016; C. Liu et al. 2017; M. Mosleh et al. 2017; W. Wang et al. 2017; K. A. Suess et al. 2019a; T. B. Miller et al. 2023; A. van der Wel et al. 2024). Furthermore, the ratio of $R_{e,\mathrm{mass}}/R_{e,\mathrm{light}}$ generally declines toward lower redshifts, introducing a substantial discrepancy between half-mass/NIR radii and optical half-light radii at later cosmic times, especially for higher-mass galaxies (M. Mosleh et al. 2017; K. A. Suess et al. 2019a, 2019b; H. Ibarra-Medel et al. 2022; T. B. Miller et al. 2023; A. van der Wel et al. 2024).

Recent studies have shown that the redshift variations of $R_{e,\mathrm{mass}}/R_{e,\mathrm{light}}$ can alter the evolutionary trend, causing mass-based radii to predict slower size growth than light-based radii (M. Mosleh et al. 2017; K. A. Suess et al. 2019a, 2019b; M. Mosleh et al. 2020; M. Hasheminia et al. 2022; T. B. Miller et al. 2023). Fortunately, the availability of data from NASA's James Webb Space Telescope (JWST) enables the examination of not only the structure of galaxies but also the robustness of mass-based parameters estimated from the Hubble Space Telescope (HST) images. A. van der Wel et al. (2024) demonstrated that average half-light sizes are up to 40% smaller in NIR wavelengths than in optical bands, while NIR radii agree well with half-mass sizes. Furthermore, examining JWST data has revealed that SFGs' sizes evolve at a slower pace in NIR relative to UV/optical (T. Morishita et al. 2024; R. G. Varadaraj et al. 2024; E. Ward et al. 2024). R. G. Varadaraj et al. (2024) measured a slope of 0.6 for Lyman break galaxies (LBGs) at $3 < z < 5$, which is aligned with the slow growth in sizes of LBGs observed by T. Morishita et al. (2024) across a wide range of $z = 5$–14.

Given the existing disagreements, it becomes crucial to carefully consider the selection method and measurement approach when examining the size evolution of galaxies.

Moreover, some recent studies have suggested that the evolution of half-mass sizes appears to be more rapid in simulations compared to that estimated from observations (K. A. Suess et al. 2019b; J. van de Sande et al. 2019; M. Hasheminia et al. 2022; T. B. Miller et al. 2023). Therefore, it is imperative to undertake more extensive analyses to examine this discrepancy between observations and simulations. Thus, we were motivated to explore the size evolution of SFGs by tracking the variations in progenitors' mass-based radii over different redshifts. In the present study, we attempt to explore the stellar mass accumulation and size evolution of SFGs by extending our previous work to the intermediate stellar mass range of $10^{10.3}$–10^{11} $M_{\odot}$. To achieve this, we utilize the structural parameters, such as semimajor and circularized radii and Sérsic index, along with the stellar mass surface density and sSFR profiles. These parameters are estimated from the stellar mass maps, allowing for a more direct comparison between observations and simulations. To properly analyze the evolution of each galaxy, we endeavor to trace it over time by identifying probable progenitors from high redshift to the local Universe.

This paper is set out as follows: Section 2 describes the data set and how we trace the progenitors and select the samples. The analyses of the evolution of mass-based structural parameters and profiles of the stellar mass and SFR are presented in Section 3. Finally, we discuss and summarize our results in Sections 4 and 5. Throughout this paper, we employed the standard cosmological parameters of $\Omega_m = 0.3$, $\Omega_\Lambda = 0.7$, and $H_0 = 70$ km s^{-1} Mpc^{-1}. Furthermore, the term "mass" refers to the stellar mass unless explicitly mentioned.

2. Data and Method

2.1. Data

In this work, our primary objective is to explore the mass-based structural evolution of intermediate-mass SFGs using the data from the 3D-HST (G. B. Brammer et al. 2012; R. E. Skelton et al. 2014; I. Momcheva 2016) over five CANDELS high-redshift fields: AEGIS, COSMOS, GOODS-N, GOODS-S, and UDS (N. A. Grogin et al. 2011; A. M. Koekemoer et al. 2011). In order to acquire structural parameters based on stellar mass maps, we matched our data set with the stellar-mass-weighted catalog generated by M. Mosleh et al. (2020). By employing a pixel-by-pixel spectral energy distribution (SED) fitting technique on the 3D-HST imaging data, M. Mosleh et al. (2020) created a collection of resolved stellar mass maps and quantified the structural parameters of 5557 galaxies. Additionally, they constructed a catalog of approximately 3000 simulated galaxies to validate the accuracy of their methodology in measuring the mass-based parameters (for more details, see M. Mosleh et al. 2020). Their analysis underscored that the sample achieved a 90% mass completeness for SFGs with $\log(M_*/M_{\odot}) \geqslant 9.8$ within the redshift range of 0.2–2.

In addition, we used the light- and mass-based parameters of the local galaxies from the Sloan Digital Sky Survey (SDSS) data set derived by M. Mosleh et al. (2017) as a reference sample at $z \sim 0$ to pose further constraints on the estimated structural evolution of selected SFGs. M. Mosleh et al. (2017) calculated the structural parameters of about 1000 random local galaxies selected from the SDSS DR7 images at $0.03 < z < 0.06$ (K. N. Abazajian et al. 2009). They measured the 1D light profiles by fitting a single Sérsic profile to the 2D surface brightness of each galaxy using GALFIT (C. Y. Peng et al. 2010). Then, by the SED fitting at each radius, they obtained the radial stellar mass and converted the light profiles to the mass profiles to estimate the light- and mass-based parameters like the Sérsic index and half-mass radius.

2.2. Sample Selection

The first step in examining the structural evolution of intermediate-to-high-mass SFGs is to select galaxies that resemble the progenitors of these SFGs at each redshift. This requires that the stellar mass of the descendants should be determined in advance. Theoretically, it has been found that SF reaches maximum efficiency around a halo mass of 10^{12} $M_{\odot}$, which corresponds to a stellar mass of $10^{10.6}$ $M_{\odot}$. This pivot mass might represent the transition point from the in situ SF-dominated regime to the merger-dominated regime (A. Dekel & Y. Birnboim 2006; L. A. Mowla et al. 2019; L. Kawinwanichakij et al. 2021). Therefore, we were motivated to study SFGs with the current stellar mass ($M_{*,0}$) around this pivot mass: two samples with $\log(M_{*,0}/M_{\odot}) = 10.3$ and 10.5, plus two more massive samples with $\log(M_{*,0}/M_{\odot}) = 10.7$ and 11. Next, it is possible to trace the main progenitors of a galaxy with a given final mass by estimating its SMGH. In this work, we obtained the SMGHs from two methods: the main-sequence integration (MSI) algorithm developed by A. Renzini (2009) and S. N. Leitner & A. V. Kravtsov (2011), which is referred to as Method I, and the average SMGH of selected disk-dominated SFGs from the IllustrisTNG (TNG50) simulations (D. Nelson et al. 2019; A. Pillepich et al. 2019), hereafter called Method II.

In Method I, we suppose that if the SFGs had relatively steady and in situ SF histories (SFHs), they evolve along the observed star-forming main sequence (MS) at each redshift. According to this method, if the local SFGs have always been star-forming in the past, at each time step their stellar mass has been accumulated by in situ SF and recycled to the interstellar medium by mass loss (ML). Therefore, by integrating the rate of mass growth (SF–ML) over time steps backward in time from the look-back time $t_0 = t(z = 0)$, it becomes possible to reconstruct the SMGH and SFH of a galaxy using its present-day stellar mass ($M_*(t_0)$):

$$M_*(t) = M_*(t_0) - \int_{t_0}^{t} (\psi(M_*, t) - \Re)\, dt. \quad (1)$$

Here $\psi(M_*, t)$ is the instantaneous SFR, and $\Re$ is the ML rate (MLR), defined as

$$\Re(t) = \int_{t_0}^{t} \Phi(t') \dot{f}_{\rm ml}(t - t')\, dt', \quad (2)$$

where $\Phi(t)$ is the SFH of this galaxy, given by

$$\Phi(t) = \psi(M_*(t), z), \quad (3)$$

and $\dot{f}_{\rm ml}$ is the fractional MLR, which is quantified by S. N. Leitner & A. V. Kravtsov (2011) as

$$f_{\rm ml} = C_0 \ln\left(\frac{t_2 - t_1}{\lambda} + 1\right), \quad (4)$$

where $C_0 = 0.046$ and $\lambda = 2.76 \times 10^5$ yr for a simple stellar population with a G. Chabrier (2003) initial mass function. Since SFH is required to estimate $\Re$, but reconstruction of $\Phi(t)$ relies on knowing the MLR, an iterative approach was

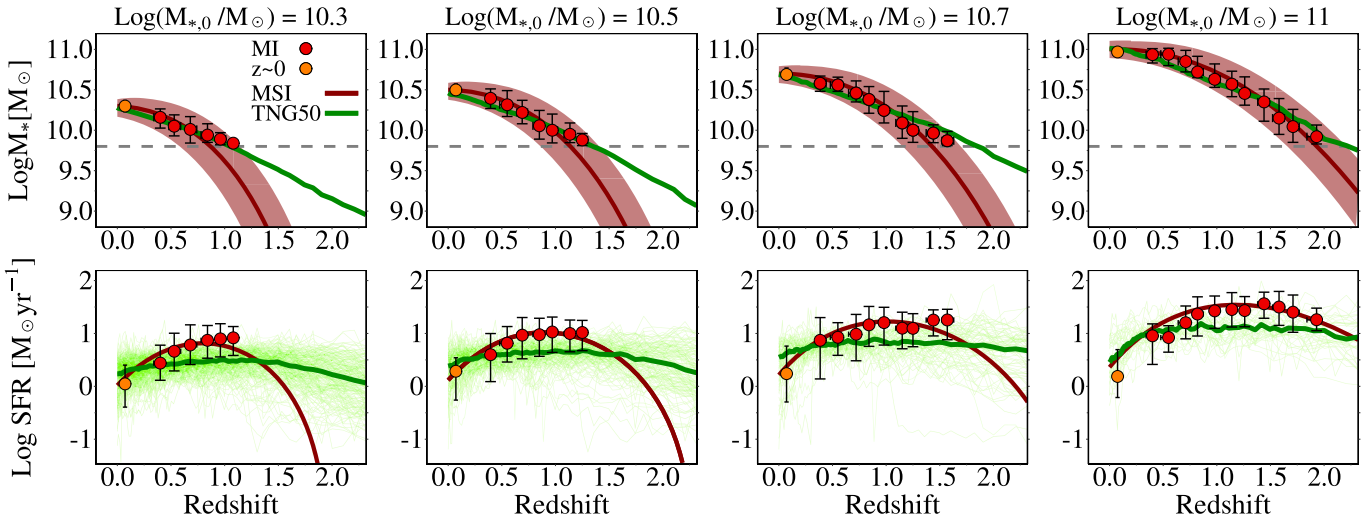

Figure 1. From left to right, mass growth histories (top) and SFHs (bottom) of SFGs with a final stellar mass of $M_{*,0} = 10^{10.3}$, $10^{10.5}$, $10^{10.7}$, and 10^{11} $M_{\odot}$ estimated by Method I (dark-red lines) using the SFR–mass relation of J. S. Speagle et al. (2014) and those selected from the IllustrisTNG (TNG50) simulations (thin light-green lines, with the median in thick green lines). The dark-red shaded areas map the thresholds utilized to choose the samples based on SMGHs. The red circles are the median values of selected galaxies from Method I, whereas the orange circles represent the sample of local SFGs provided by M. Mosleh et al. (2017) using the SDSS DR7 images. In addition, the dashed gray lines visually illustrate the stellar mass limit of our primary sample, from the catalog of M. Mosleh et al. (2020).

presented by S. N. Leitner & A. V. Kravtsov (2011) to solve this problem. In this method, by assuming an initial value of $\Re = 0.45$, Equation (1) is solved over each time interval. This allows us to estimate the SFR and mass of a galaxy step by step until reaching around its formation time. Subsequently, by employing the derived SFH, we can reassess the $\Re$ at each step. This process is reiterated multiple times to ensure that the results converge and are reliable.

To estimate the instantaneous SFR of galaxies, we adapted the SFR–M_* relation of J. S. Speagle et al. (2014), which is calculated based on the compilation of 64 MS relations from 25 studies at $z = [0, 6]$:

$$\log \psi(M_*, t) = (0.84 - 0.026 \times t)\log M_* - (6.51 - 0.11 \times t), \quad (5)$$

where t is the age of the Universe (in Gyr).

We selected the galaxies as progenitors whose mass and redshift reside, respectively, within ± 0.1 dex and ± 0.2 of derived stellar mass assemblies to account for the uncertainties in estimating the stellar mass of observed galaxies and errors in calculating SMGHs. We adopted the U–V versus V–J (R. J. Williams et al. 2009) rest-frame color criterion given in M. Mosleh et al. (2017) to distinguish SFGs from QGs. The galaxies with unreliable parameters (~16%; see Section 2.3) were eliminated. Our final sample consists of 778, 1229, 1262, and 906 galaxies as possible progenitors of SFGs with a present-day stellar mass of $10^{10.3}$, $10^{10.5}$, $10^{10.7}$, and 10^{11} $M_{\odot}$, respectively, using Method I over a redshift range of $z = [0.3–2]$.

For a reference sample at $z \sim 0$, we chose the SDSS local SFGs with a stellar mass similar to the final mass of studied galaxies ($M_{*,0}$) in order to obtain more accurate fits. To do this, we picked SFGs from the sample of M. Mosleh et al. (2017) with the final mass of $\log(M_*/M_{\odot}) = \log(M_{*,0}/M_{\odot}) \pm 0.1$ dex. By applying this threshold, 146, 114, 83, and 28 local galaxies are chosen as local SFGs with $\log(M_*/M_{\odot}) = 10.3 - 11$. In Figure 1, the red circles illustrate the median of stellar mass and SFR of progenitors derived from Method I over $0.3 < z < 2.0$, whereas the local SFGs are shown with orange circles. The error bars represent the 16th–84th percentiles of the distribution for each sample of galaxies. As can be seen, there is a slight difference in the estimated stellar mass between MSI and the observed median values from Method I for $\log(M_*/M_{\odot}) < 10$. Given that our observational data have a mass limit of $\log(M_*/M_{\odot}) = 9.8$, by imposing the mass and redshift thresholds of ± 0.1 dex and ± 0.2, respectively, the median mass of the selected samples may exceed the MSI estimation at higher redshifts.

To ensure that sample selection based on the MSI mass growth in which the merger effect is neglected does not significantly alter our findings, as well as for a more accurate comparison with simulations, we attempted to obtain the mass assembly histories of SFGs using the SMGH calculated by the IllustrisTNG simulations. This paper uses the results of the smallest-volume and highest-resolution version of the IllustrisTNG Project, TNG50-1 (D. Nelson et al. 2019; A. Pillepich et al. 2019). To select the local SFGs with a specific final mass, the following thresholds were applied to galaxies at $z = 0$ (snapshot 99):

1. Stellar mass within the radius of 30 kpc (C. Engler et al. 2021): $\log(M_*/M_{\odot}) = \log(M_{*,0}/M_{\odot}) \pm 0.15$ dex.
2. Disk-to-total ratio obtained by classification 1 (see M. Du et al. 2020) for stars within 30 kpc: $D/T > 0.5$.
3. SFR within a sphere of radius 30 kpc averaged across the past 100 Myr (M. Donnari et al. 2019; A. Pillepich et al. 2019): $\mathrm{SFR}(M_{\odot}\,\mathrm{yr}^{-1}) = [0.1, 10.0]$.

With these thresholds, 209, 142, 77, and 37 galaxies were selected in TNG50-1 as counterparts of disk-dominated SFGs with a final mass of $10^{10.3}$, $10^{10.5}$, $10^{10.7}$, and 10^{11} $M_{\odot}$, respectively. We then used the `SubLink` merger tree of the IllustrisTNG simulation (V. Rodriguez-Gomez et al. 2015) to link the (sub)halos at different snapshots and extract the main progenitor branch for individual galaxies. The full assembly history of each parameter for an SFG with a given present-day

mass is derived by calculating the median values from a sample of entire progenitors of selected galaxies with the same mass at $z = 0$. The obtained median mass is defined as the estimated SMGH from the TNG simulation, represented by the green line in Figure 1. Using these SMGHs and applying the previous criteria, we selected 877, 1145, 1059, and 806 observed galaxies as the probable progenitors of Method II.

As seen in Figure 1, the TNG simulations predict a slower mass growth rate than Method I, especially for masses less than $\log(M_*/M_\odot) \sim 9.9$. This discrepancy may result from not considering the merger or inaccurate ML rates or SFRs in the MSI. However, as the minimum mass of our sample is $10^{9.8}$ $M_\odot$, we can argue that the SMGHs obtained from both methods do not differ significantly within the data range of this study. In addition, the lower SFR values observed in TNG50 suggest that different SMGHs may arise from the MSI initial assumption, which may not consistently hold, as SFGs may have gone through quenching periods during their evolution. To explore the impact of such events on mass accumulation and SFR, we identified quenched galaxies within the TNG simulation. By applying the sSFR thresholds of $\mathrm{sSFR}(z) < 1/(6 \times t_H(z))$ (as defined by S. Tacchella et al. 2019), we found that, on average, approximately 10% of present-day SFGs in our TNG samples underwent a phase of quenching throughout their lifetime. Thus, experiencing a quenching period during the evolution can also contribute to the dissimilarity between the predicted SMGHs of Method I and TNG simulations. However, this difference might not be notable, at least when considering the galaxies within the low-to-intermediate-mass range.

Given the similar SFHs for simulated samples with and without ones with quenching periods, it appears that the lower SFR values in TNG50 compared to the MSI and observations could not be attributed to the existence of quenching phases during the evolution of SFGs. A similar discrepancy in the normalization values of MS between TNG and observational data was also reported by M. Donnari et al. (2019). They found that while TNG simulations have marginally higher SFR at $z = 0$, their predictions are $\sim$0.2–0.5 dex lower than observational measurements (including J. S. Speagle et al. 2014) at intermediate redshifts.

2.3. Size Measurement

The mass-based sizes provided by M. Mosleh et al. (2020) are circularized, which is determined from the semimajor axis ($r_{e,\mathrm{SMA}}$) and the axis ratio (b/a) by $r_{e,\mathrm{cir}} = r_{e,\mathrm{SMA}}\sqrt{b/a}$, to remove the effects of ellipticity. However, for SFGs or disk galaxies, the semimajor-axis sizes of the ellipse that contains half of the total fluxes (total masses in this work) are often used (see, e.g., A. van der Wel et al. 2014). Therefore, to adopt the standard measurement of half-mass radius along the semimajor axis and to assess the evolution of size and compare with previous studies, the size measurements were redone using 1D stellar mass surface density profiles derived from the stellar mass maps provided by M. Mosleh et al. (2020). This approach reduces the effects of uncertainties in the mass maps, particularly in the outer regions of the galaxies. The procedure is nearly similar to the first size measurement method used in M. Mosleh et al. (2020), which followed D. T. Maltby et al. (2018).

In short, we first need to find the best-fit Sérsic models from their 1D stellar mass surface density profiles. The 1D profiles were obtained using the IRAF task ELLIPSE (R. I. Jedrzejewski 1987). However, to ensure consistency in the semimajor-axis size $r_{e,\mathrm{SMA}}$ with other studies, this process must be conducted in fixed-parameter mode, where the axis ratio (b/a) and position angle (PA) are held constant during the ELLIPSE fitting procedure. Finding the best fixed parameters from the stellar mass maps is more challenging. To address this, we utilized the output from the free-parameter mode (i.e., b/a, PA, and the circularized effective radius $r_{e,\mathrm{cir}}$ from M. Mosleh et al. 2020) to estimate the appropriate b/a and PA values for the fixed-parameter mode. We calculated the average b/a values from the radial profiles within a radius range of 2 times $r_{e,\mathrm{cir}}$ to the radius where the stellar mass radial density profile reaches 10^7 $M_\odot\,\mathrm{kpc}^{-2}$, beyond which background noise becomes dominant. We followed M. Mosleh et al. (2020) and used the simulated galaxies to ensure that the method could recover the true values. A slight correction was necessary to implement after comparing the true and measured values of the b/a, using the H_{160}-band mock galaxies. The corrected average b/a_{avg} method is then used and applied to obtain the average $\mathrm{PA}_{\mathrm{avg}}$. This method is also tested for the simulated mass maps.

After determining the average position angle ($\mathrm{PA}_{\mathrm{avg}}$) and axis ratio ($b/a_{\mathrm{avg}}$) and fixing the center, we obtained the stellar mass radial density profile using a fixed-parameter mode. In the next step, we generated a library of 1D Sérsic models for finding the best-fitting ones. Specifically, we used GALFIT (C. Y. Peng et al. 2010) to first create 2D models on a grid spanning the size–Sérsic parameter space. The decision to generate 2D Sérsic models first and then derive the library of 1D profiles was driven by two key considerations. First, this approach allows us to account for the 2D distribution of the point-spread function (PSF), which can significantly affect the profiles. By fitting ellipses to the PSF-convolved 2D models (with fixed center, PA, and ellipticity), we ensure that the resulting 1D profiles accurately reflect the impact of the PSF, thereby providing a more accurate comparison with observed data. Second, generating 1D profiles from 2D models ensures consistency with the observed data. Both the model and observed profiles undergo the same ellipse-fitting process, which minimizes potential biases that could arise if the profiles were derived using different methods. This consistency is crucial for the reliability of the subsequent χ^2 minimization step, where we compare the normalized 1D mass density profiles of the galaxies with all normalized model profiles in the library to find the best-fitting model based on the minimum χ^2 values.

The robustness of the measurements was examined by utilizing simulated galaxies. Based on the results from the simulated mass maps, we found that on average the Sérsic indices were underestimated by about 30%, while the $r_{e,\mathrm{SMA}}$ at $z \gtrsim 1.2$ were overestimated by 25%. Therefore, we have corrected these parameters, based on the outputs of these simulations.

3. Results

In this section, we examine how the structure of intermediate-mass SFGs changes with redshift, by analyzing the evolution of structural parameters such as size, Sérsic index (n), axis ratio (b/a), and stellar mass surface density within a radius of 1 kpc (Σ_1). We also compare radial profiles of stellar mass and sSFR of our samples.

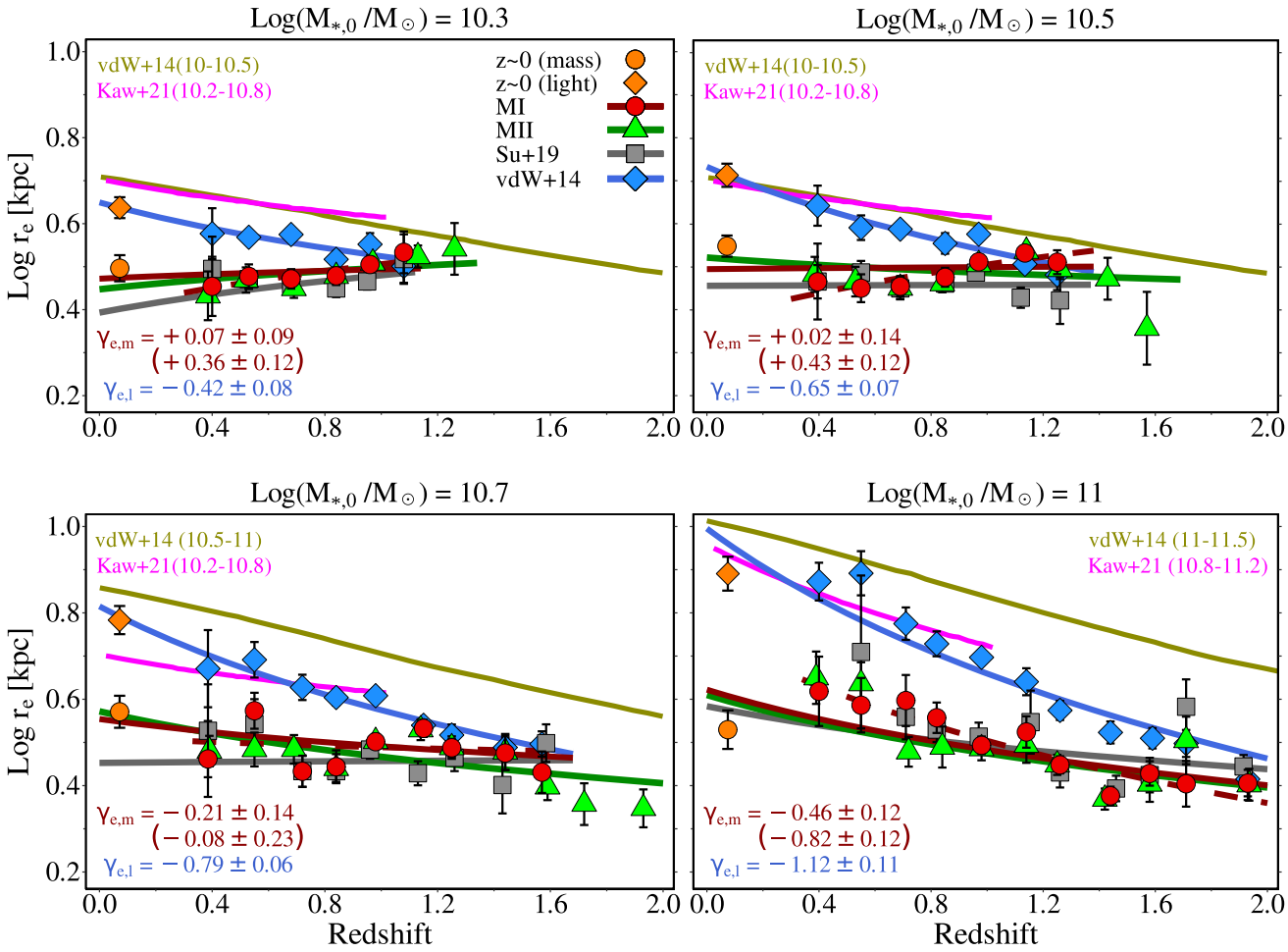

Figure 2. Redshift evolution of effective radius $r_{e,\mathrm{SMA}}$ for progenitors of the SFGs at different stellar mass bins. The dark–red and green lines represent the best fit to the medians of the form $r \propto (1+z)^{\gamma}$ inferred from Method I (red circles) and Method II (green triangles), respectively, while the dark-red dashed lines show the fit to the median size evolution of Method I without considering the sizes at $z \sim 0$. The half-mass and half-light radii of the local SDSS samples, obtained from M. Mosleh et al. (2017), are shown by orange circles and diamonds, respectively. The median sizes (best fit) estimated by K. A. Suess et al. (2019a) and A. van der Wel et al. (2014) are shown with gray squares (gray line) and blue diamonds (blue line), respectively. The best-fit slopes derived from Method I (with and without the local data) and light-based sizes of A. van der Wel et al. (2014) are denoted in dark red (without and with parentheses) and blue, respectively. As seen, the mass-based radii (K. A. Suess et al. 2019a) are in good agreement with our sizes, while $r_{e,\mathrm{light}}$ (A. van der Wel et al. 2014) is greater than $r_{e,\mathrm{mass}}$, especially at higher redshifts. For comparison, the size evolutions obtained by A. van der Wel et al. (2014; olive line) and L. Kawinwanichakij et al. (2021; magenta line) for SFGs at fixed masses are overplotted.

3.1. Size Growth

The effective radius ($r_{e,\mathrm{SMA}}$) evolution of progenitors with $\log(M_{*,0}/M_{\odot}) = 10.3 - 11$ is shown in Figure 2. Dark-red and green lines represent the fit of the form $r \propto (1+z)^{\gamma}$ to the median size inferred from Methods I and II, respectively. To fulfill this, we calculated the fit on the median of samples selected using Method I (red circles) and Method II (green triangles) in 11 redshift bins from $z = 2.0$ to $z = 0.3$ and the median of SDSS local SFGs (orange circles from M. Mosleh et al. 2017). The best fits to the median data obtained from Method I, with and without considering the SDSS data, are shown with solid and dashed dark-red lines, respectively. The uncertainty in each bin is derived from bootstrap resampling.

According to Figure 2, from $z = 2.0$ to $z = 0$, the progenitors of massive galaxies ($\log(M_{*,0}/M_{\odot}) = 11.0$) have a relatively slow evolution in size with $\gamma_{\mathrm{MI}} = -0.46 \pm 0.12$ and $\gamma_{\mathrm{MII}} = -0.45 \pm 0.14$, while the growth rate for both methods is much higher when local SDSS data are not considered. We can also observe a similar difference in growth rates of other parameters in our massive sample with and without considering $z = 0$, possibly due to the following reasons: Our SDSS sample has only 28 galaxies with $\log(M_{*,0}/M_{\odot}) = 11.0$, which leads to significant scatter in the median of structural parameters. The next problem is that the parameter measurement method differs in SDSS and 3D-HST/CANDELS data. For SDSS galaxies at a redshift of $z \sim 0$, the light profiles were first derived by fitting single Sérsic models to the observed 2D surface brightness images in different filters using `GALFIT`. From these best-fit models, the 1D light profiles are extracted for various filters, and these light profiles were then used to derive the deconvolved stellar mass profiles by performing SED fitting at each radial bin. Finally, the half-mass radius and other parameters were obtained from the stellar mass profiles (see M. Mosleh et al. 2017, for more details). Meanwhile, for galaxies in CANDELS fields, 2D stellar mass maps were calculated directly by fitting the best SED model for each pixel. After that, using `IRAF/ELLIPSE`, the stellar mass surface density profiles were estimated from the mass maps to derive the structural parameters. This leads to a slight mismatch

Table 1
Slopes of the Median Size Evolution (γ) for Different Radii

$\log(M_{*,0}/M_{\odot})$	Size	Method I (w/o z $\sim$ 0)	Method II	Sizes from Su+19	Sizes from vdW+14
10.3	r_{20}	0.40 ± 0.14 (0.64 ± 0.23)	0.39 ± 0.12	0.45 ± 0.14	-0.07 ± 0.07
	r_e	0.07 ± 0.09 (0.36 ± 0.12)	0.17 ± 0.12	0.29 ± 0.36	-0.42 ± 0.08
	r_{80}	-0.13 ± 0.13 (0.09 ± 0.27)	-0.01 ± 0.13	-0.54 ± 0.07	-0.74 ± 0.06
10.5	r_{20}	0.30 ± 0.24 (0.87 ± 0.14)	0.11 ± 0.15	-0.01 ± 0.16	-0.35 ± 0.11
	r_e	0.02 ± 0.14 (0.43 ± 0.12)	-0.12 ± 0.13	0.01 ± 0.29	-0.65 ± 0.07
	r_{80}	-0.14 ± 0.13 (-0.03 ± 0.23)	-0.26 ± 0.13	-0.61 ± 0.06	-0.94 ± 0.04
10.7	r_{20}	0.08 ± 0.22 (0.58 ± 0.22)	-0.13 ± 0.14	-0.10 ± 0.14	-0.50 ± 0.10
	r_e	-0.21 ± 0.14 (-0.08 ± 0.22)	-0.35 ± 0.11	0.02 ± 0.25	-0.79 ± 0.06
	r_{80}	-0.36 ± 0.14 (-0.45 ± 0.22)	-0.53 ± 0.12	-0.74 ± 0.12	-1.10 ± 0.09
11.0	r_{20}	-0.18 ± 0.12 (-0.03 ± 0.15)	-0.19 ± 0.14	-0.04 ± 0.22	-0.82 ± 0.07
	r_e	-0.46 ± 0.12 (-0.82 ± 0.12)	-0.45 ± 0.14	-0.36 ± 0.29	-1.12 ± 0.11
	r_{80}	-0.99 ± 0.21 (-1.57 ± 0.13)	-1.02 ± 0.24	-0.85 ± 0.19	-1.37 ± 0.17

between the parameters obtained by these two different methods and packages.

For SFGs with $\log(M_{*,0}/M_{\odot}) = 10.7$, the effective radius does not significantly change over the redshift range of $0 < z < 2$ with $\gamma_{\rm MI} = -0.21 \pm 0.14$ and $\gamma_{\rm MII} = -0.35 \pm 0.11$. The median trend lines are reversed for galaxies with a mass below the pivot mass, although this size reduction is slightly noticeable when we exclude local galaxies in the analysis. In general, from $z \sim 1.5$ to the current epoch, samples with $\log(M_{*,0}/M_{\odot}) \lesssim 10.7$ have a growth rate close to zero; hence, it is reasonable to conclude that their sizes remain almost constant throughout cosmic time. However, this trend marginally differs for SFGs with $\log(M_{*,0}/M_{\odot}) = 11$. We note that despite the approximately different slopes estimated with and without the local data, the median size evolution of galaxies follows a similar trend regarding the stellar mass. In addition, the results are consistent using Method II for selecting the progenitor and considering mergers in the SMGHs (green lines and best-fit values in Table 1). Only progenitors of $\log(M_{*,0}/M_{\odot}) = 10.7$ at $z \sim 1.5$–2 have smaller sizes; consequently, the effective radius increases slightly at this epoch.

To check our findings with other mass- and light-based measurements, we cross-matched our data with size catalogs provided by K. A. Suess et al. (2019a) and A. van der Wel et al. (2014). The median evolution of the half-mass radius from K. A. Suess et al. (2019a; gray squares) and the half-light size from A. van der Wel et al. (2014; blue diamonds) are shown as gray and blue trend lines in Figure 2, respectively. Our half-mass radii almost agree with those estimated by K. A. Suess et al. (2019a), except for some intervals, where there is considerable uncertainty in the median owing to the small number of selected galaxies. The difference in these bins, as well as the lack of parameters for local galaxies, has caused the estimated slope for data from K. A. Suess et al. (2019a) to be slightly different from what we found, particularly for the two lower-mass samples. Nevertheless, the general trend does not alter concerning our size measurements, and the results are consistent. However, the $r_{e,\rm light}$ of A. van der Wel et al. (2014) is larger than $r_{e,\rm mass}$, especially at low redshifts, which is in line with previous works suggesting that the average half-mass radii of galaxies are smaller than their half-light radii (D. Szomoru et al. 2013; M. Mosleh et al. 2017, 2020; K. A. Suess et al. 2019b; T. B. Miller et al. 2023; A. van der Wel et al. 2024). As a result, the growth rates of light-based sizes become steeper, which is more notable in high-mass samples.

We also plotted the evolution of half-light sizes from A. van der Wel et al. (2014; olive lines) for SFGs at a fixed mass of $\log(M_*/M_{\odot})$= 10–10.5 (-0.52 ± 0.08), 10.5–11 (-0.72 ± 0.09), and 11–11.5 (-0.80 ± 0.18) and from L. Kawinwanichakij et al. (2021; magenta lines) with $\log(M_*/M_{\odot})$= 10.2–10.8 (-0.29 ± 0.01) and 10.8–11.2 (-0.77 ± 0.02). It can be seen from Figure 2 that the sizes of galaxies at fixed mass are larger than those inferred from the sample selected as progenitors of a given galaxy, even if we use the same data (half-light radii adopted from A. van der Wel et al. 2014).

Moreover, we applied additional measurements of r_{20} and r_{80}, representing the radii that contain 20% and 80% of a galaxy's total stellar mass, respectively. The evolution in the median r_{20} and r_{80} of our samples is shown in the top and bottom panels of Figure 3, respectively. Although the slope of size growth of Method I decreases when considering the local samples, in general the evolution of Method I is consistent with those derived by Method II within the errors. The r_{20} size of massive galaxies slightly grows since $z \sim 2.0$, from which it can therefore be inferred that the mass fraction inside these regions remains approximately constant. In contrast, the r_{20} radii of other samples decrease toward low redshift, especially for $z < 1.2$. It can be concluded that the stellar mass grows faster in the central parts of these galaxies, which leads to the r_{20} radius reaching about 1 kpc in $z \sim 0.3$.

Finally, using r_{80}, the size of massive SFGs grows toward low redshifts, which leads to the largest r_{80} for SFGs with $\log(M_{*,0}/M_{\odot}) = 11$ at later epochs. For lower-mass samples, this rate slows down, so that for the progenitors with $\log(M_{*,0}/M_{\odot}) = 10.5$ it can be seen that the slope is closely flat for both methods. These trends between the stellar mass of galaxies and their sizes seem to indicate that the mass growth in the massive galaxies is relatively faster in the outskirts, unlike the low-mass SFGs, in which mass builds up at a higher rate in the interior regions. For intermediate-mass galaxies with masses around the pivot mass, mass growth rates in the inner and outer parts are relatively comparable; therefore, these SFGs evolve self-similarly, as inferred from the evolution of half-mass radius.

For comparison with the mass- and light-based sizes of K. A. Suess et al. (2019a) and A. van der Wel et al. (2014), we tried to estimate r_{20} and r_{80} from n and r_e of their catalogs using

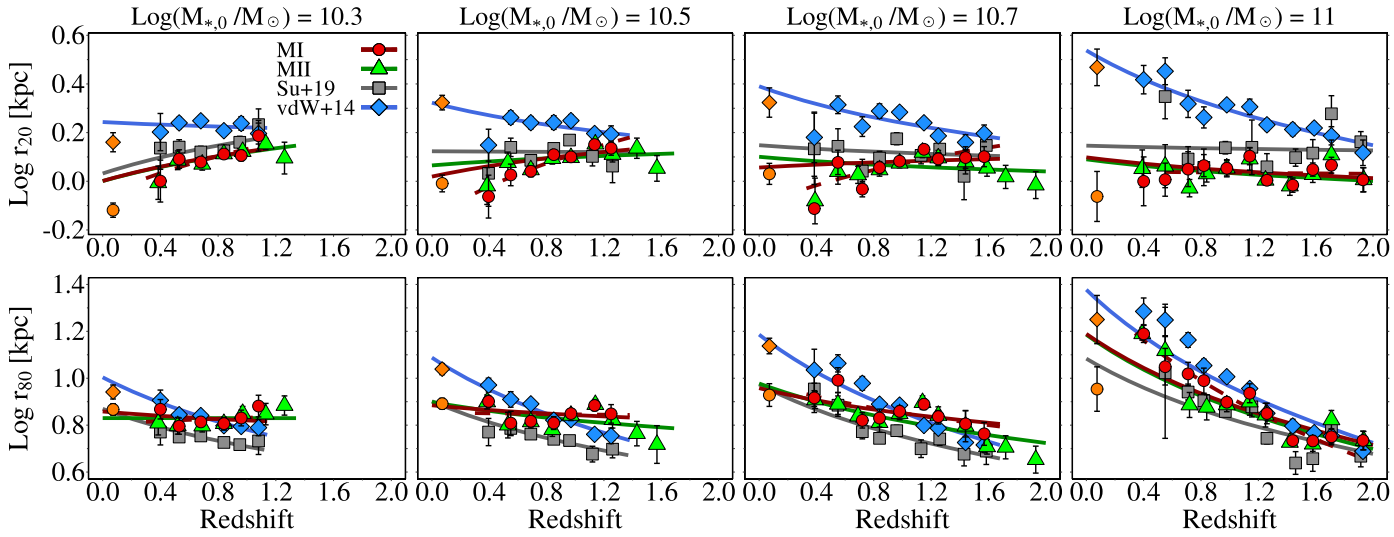

Figure 3. Evolution in the median of r_{20} (top) and r_{80} (bottom) of SFGs, as in Figure 2. The r_{80} sizes of the progenitors of higher-mass SFGs have grown more than those with lower final mass, while their r_{20} remains relatively constant. In contrast, the r_{20} of smaller mass samples decreases with time, compared to the most massive SFGs, which have almost constant r_{20} sizes. These results differ from the r_{20} and r_{80} estimated from the size catalogs of K. A. Suess et al. (2019a) and A. van der Wel et al. (2014), which is probably related to the difference in Sérsic index and $r_{e,\mathrm{light}}$ (for A. van der Wel et al. 2014) (see text for more details).

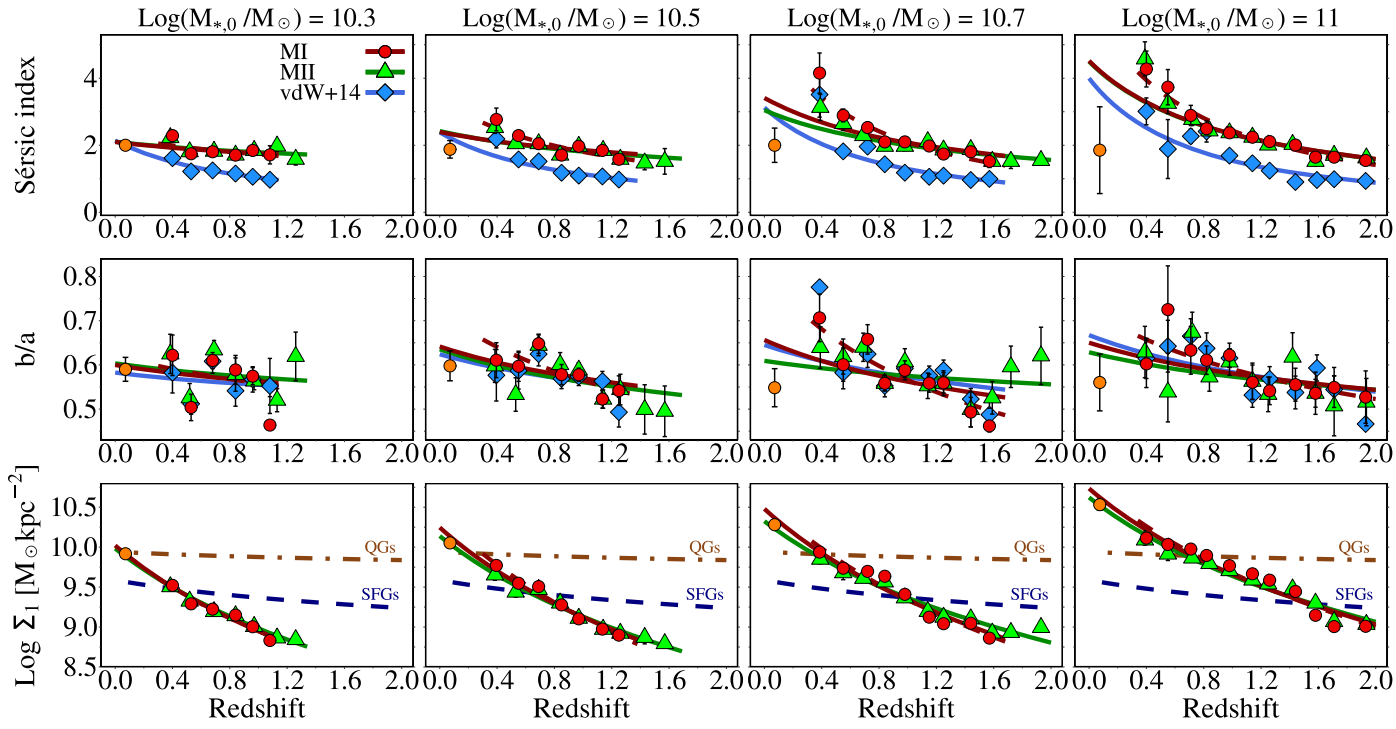

Figure 4. From top to bottom, redshift evolution of Sérsic index (n), axis ratio (b/a), and central stellar mass density (Σ_1), as in Figure 2. The dashed navy and dashed–dotted brown lines in the bottom panels represent the fit to all SFGs and QGs, respectively, in our primary sample. It should be noted that A. van der Wel et al. (2014) fitted single Sérsic models to the light profiles to measure the parameters; therefore, the estimated n is smaller than the ones found using the mass profiles.

Equation (3) of T. B. Miller et al. (2019). It is important to note that the Sérsic indices from the A. van der Wel et al. (2014) catalog, adopted by K. A. Suess et al. (2019a) as well, were derived from the light profiles and are smaller than those measured by M. Mosleh et al. (2020) using mass profiles. Therefore, the r_{20} radii obtained from the structural parameters of K. A. Suess et al. (2019a) and A. van der Wel et al. (2014) are larger than what we found. By contrast, since r_{80} is proportional to n, the r_{80} sizes from the parameters of the K. A. Suess et al. (2019a) catalog are smaller than our measurements. In comparison, the r_{80} radii of A. van der Wel et al. (2014) are approximately consistent with our sizes because of the larger values of half-light radii than half-mass radii.

3.2. Morphological Evolution of Progenitors

In the top panel of Figure 4, the evolution of the median Sérsic index (n) is illustrated for progenitors tracked via Method I (with and without $z \sim 0$) and Method II, as well as

Table 2
The Best-fit Parameters for the Structural Evolution of the Same Samples as in Table 1

$\log(M_{*,0}/M_{\odot})$	Parameter	Method I (w/o $z\sim0$)	Method II	Data from vdW+14
	n	-0.26 ± 0.17 (-0.40 ± 0.31)	-0.23 ± 0.14	$-1.05\ \pm\ 0.09$
10.3	b/a	-0.09 ± 0.16 (-0.16 ± 0.34)	-0.08 ± 0.12	-0.07 ± 0.11
	Σ_1	-3.56 ± 0.22 (-3.52 ± 0.42)	-3.33 ± 0.14	...
	n	-0.37 ± 0.24 (-0.91 ± 0.25)	-0.42 ± 0.17	-1.08 ± 0.21
10.5	b/a	-0.17 ± 0.10 (-0.35 ± 0.14)	-0.18 ± 0.10	-0.15 ± 0.09
	Σ_1	-3.73 ± 0.25 (-4.31 ± 0.25)	-3.36 ± 0.16	...
	n	-0.72 ± 0.27 (-1.39 ± 0.18)	-0.61 ± 0.15	-1.28 ± 0.31
10.7	b/a	-0.22 ± 0.13 (-0.52 ± 0.11)	-0.08 ± 0.08	-0.17 ± 0.13
	Σ_1	-3.79 ± 0.27 (-4.13 ± 0.36)	-3.19 ± 0.18	...
	n	-0.95 ± 0.20 (-1.35 ± 0.10)	-0.95 ± 0.21	-1.38 ± 0.24
11.0	b/a	-0.16 ± 0.08 (-0.30 ± 0.08)	-0.13 ± 0.09	-0.19 ± 0.09
	Σ_1	-3.56 ± 0.27 (-3.80 ± 0.34)	-3.26 ± 0.18	...

those cross-matched with the light profile's Sérsic indices measured by A. van der Wel et al. (2014) (see Table 2 for the values). The $z\sim0$ samples have different Sérsic indices, in particular for the massive SFGs. As previously mentioned, this disparity stems from employing dissimilar methodologies for measuring the parameters and the statistically small number of galaxies in these bins. The Sérsic index from the A. van der Wel et al. (2014) catalog exhibits lower values but a steeper slope.

In addition to n, we used the redshift evolution of central surface mass density within 1 kpc (Σ_1) to investigate the buildup of central structures. In the bottom panels of Figure 4, we display the median evolution of Σ_1 as a function of redshift for progenitors selected by Methods I and II and all SFGs and QGs in our mass-based data from $z\sim0.0$ to 2.0. As can be seen, median central densities increase significantly over the redshift range of our study. Generally, both methods have relatively consistent median slopes within their errors, even without considering data at $z\sim0$. However, the redshift evolution of Σ_1 is generally in agreement with the average increase in the Sérsic index, suggesting that the interior regions of SFGs become more concentrated and these galaxies form a dense central core (bulge or pseudobulge). The central density of our two more massive samples reaches the average values of QGs at $z\sim0.4$ and $z\sim0.8$, respectively, suggesting that the rate of evolution of a galaxy's central structure probably correlates with its stellar mass. At these epochs, the Sérsic index also increased and surpassed $n=3$, comparable to those of QGs, which agrees with the results of G. Barro et al. (2017). They found that the SFGs whose Σ_1 overlapped with QGs had Sérsic indices close to the fully quenched galaxies and exhibited a similar morphology.

Finally, we used the minor-to-major-axis ratio (b/a) to study the morphological changes of our SFGs and examine the results obtained from the evolution of n and Σ_1. The axis ratio slightly increases with cosmic time and reaches values of 0.6 and 0.7 for samples below and above, respectively, the pivoting mass in the local Universe, which are close to the mean apparent axis ratio of disk- and bulge-dominated galaxies calculated by R. A. Vincent & B. S. Ryden (2005). Using SDSS DR3 data, R. A. Vincent & B. S. Ryden (2005) studied a sample of about 96,000 galaxies and measured the mean apparent axis ratio of 0.59 and 0.74 for galaxies with pure exponential ($n\lesssim1.2$) and de Vaucouleurs profiles ($n\gtrsim3.3$), respectively.

3.3. Radial Stellar Mass Assembly

Studying the stellar mass distribution within the galaxies and comparing the mass buildup in different radii could lead to a better understanding of the stellar mass assembly in galaxies. Thus, we extend our analysis to use the stellar mass surface density profiles and track the redshift evolution of radial mass distribution for each sample in a nonparametric way. Figure 5 presents our samples' median mass density profiles within a radius of 12 kpc. To provide a more clear depiction of the profiles, they are presented in six bins. For comparison, we adopted the stellar mass density profiles of four samples of local SFGs with stellar mass $\log(M_*/M_{\odot})=10.2-11.2$, provided by M. Mosleh et al. (2017) using the SDSS DR7 images at $0.06<z<0.08$ (dark-orange lines). Olive and cyan vertical dashed lines represent radii of 2 and 6 kpc, and the gray shaded area shows the maximum half-width at half-maximum of PSFs. The majority of profiles exhibit little to no change in their general shape with redshift, and their slope remains approximately constant, suggesting that stellar mass is built up at all radii. However, for high-mass samples, stellar mass grows slightly faster in the outer parts ($6\,\mathrm{kpc}<R<12\,\mathrm{kpc}$) at high redshifts. The slope of mass density profiles tends to be shallower in these regions at $z<1.1$ for samples with $\log(M_{*,0}/M_{\odot})\geqslant10.7$. In contrast, inner mass profiles ($R<2$ kpc) become marginally steeper, which is consistent with the concentration of the central region.

We further quantified and compared the mass buildup in the different areas along with the mass density profiles. In Figure 6, olive triangles, cyan circles, and pink diamonds display the stellar mass assembled in the inner ($R<2$ kpc), middle ($2\,\mathrm{kpc}<R<6\,\mathrm{kpc}$), and outer regions ($6\,\mathrm{kpc}<R<12\,\mathrm{kpc}$), while the black squares give the total stellar mass. At $z\sim0.4$, the stellar masses within each sample's inner and middle regions have nearly the same values. This is also the same for the local galaxies, so it is reasonable to suppose that the mass distributed inside 2 kpc and 2–6 kpc is almost the same at lower redshifts. For a more accurate analysis of evolutionary rates in different regions, we have plotted the linear fit to the total mass as dotted lines in Figure 6. It is evident that the slopes of the mass assembly differ between the central and outer parts in each mass regime. The mass evolution in the inner radii of galaxies with $\log(M_{*,0}/M_{\odot})=10.3$ is somewhat faster, with 0.52 dex growth in the mass inside $R=2$ kpc, while the stellar mass added to the outer regions increased only by 0.29 dex, which confirms our findings about the size evolution of these low-mass SFGs. In addition, the central region of more massive

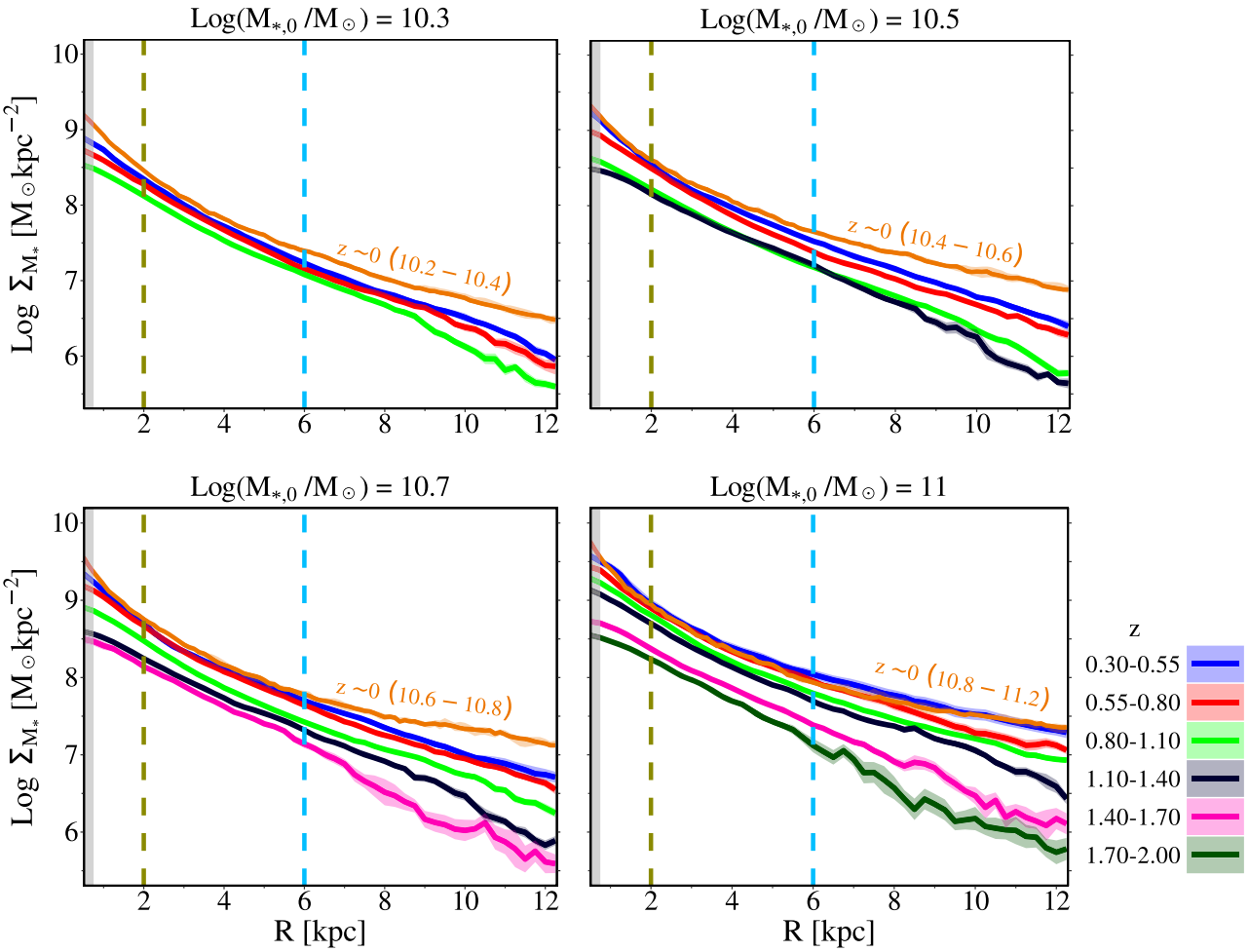

Figure 5. Stellar mass surface density profiles of SFGs with $\log(M_{*,0}/M_{\odot}) = 10.3$, 10.5, 10.7, and 11 in different redshifts, along with the profiles of the local SFGs at $z \sim 0$ calculated by M. Mosleh et al. (2017; dark-orange lines) using SDSS DR7 images. The dashed olive and cyan lines illustrate radii of 2 and 6 kpc, respectively. The slopes of profiles in the middle part (2 kpc $< R <$ 6 kpc) evolve at nearly the same rate in all redshifts, whereas toward the lower redshift slopes of the inner ($R <$ 2 kpc) and outer regions (6 kpc $< R <$ 12 kpc) increase and decrease, respectively.

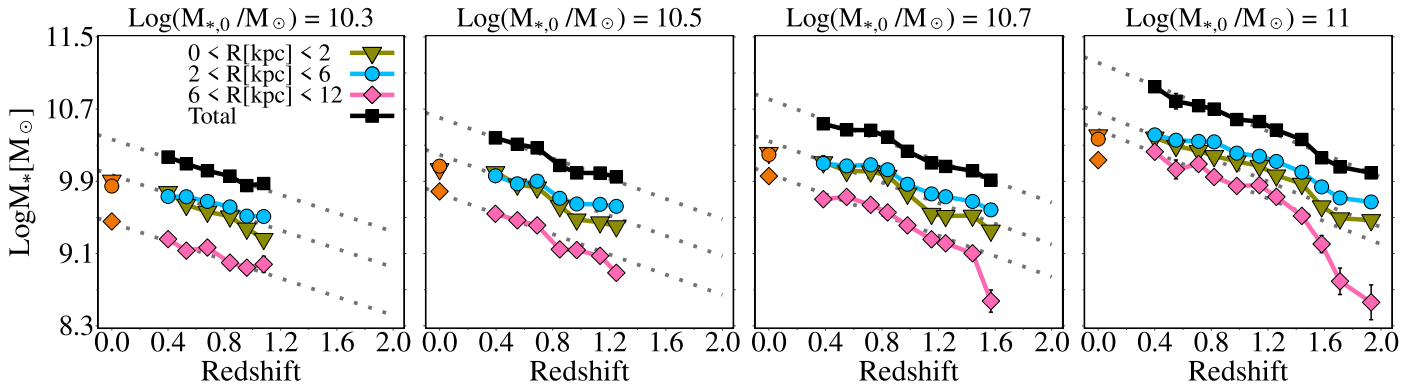

Figure 6. Mass assembly in the inner (olive triangles), middle (cyan circles), and outer (pink diamonds) regions of progenitors. The dark-orange points represent the stellar mass of the corresponding regions at $z \sim 0$, calculated from the profiles of the local SFGs derived by M. Mosleh et al. (2017). The black squares and dotted lines illustrate the total stellar mass over redshift bins and the corresponding best fits, respectively. The mass growth rate of the different regions is in line with the size and Σ_1 evolution of progenitors.

SFGs experienced a noticeable mass increase (0.47 and 0.63 dex) between $z = 1.1$–0.7 and $z = 1.7$–1.0 for progenitors with $\log(M_{*,0}/M_{\odot}) = 10.7$ and 11, respectively. The rapid mass accumulation within the core of these SFGs is consistent with the accelerated growth of their central densities (Σ_1) at these epochs. In addition, the outskirts of these galaxies had an accelerated mass growth phase at high redshifts. The stellar mass within the range 6 kpc $< R <$ 12 kpc of SFGs with $\log(M_{*,0}/M_{\odot}) = 10.7$ and 11 increased by 0.53 and 1.31 dex at $1.45 < z < 1.65$ and $1.1 < z < 2.0$.

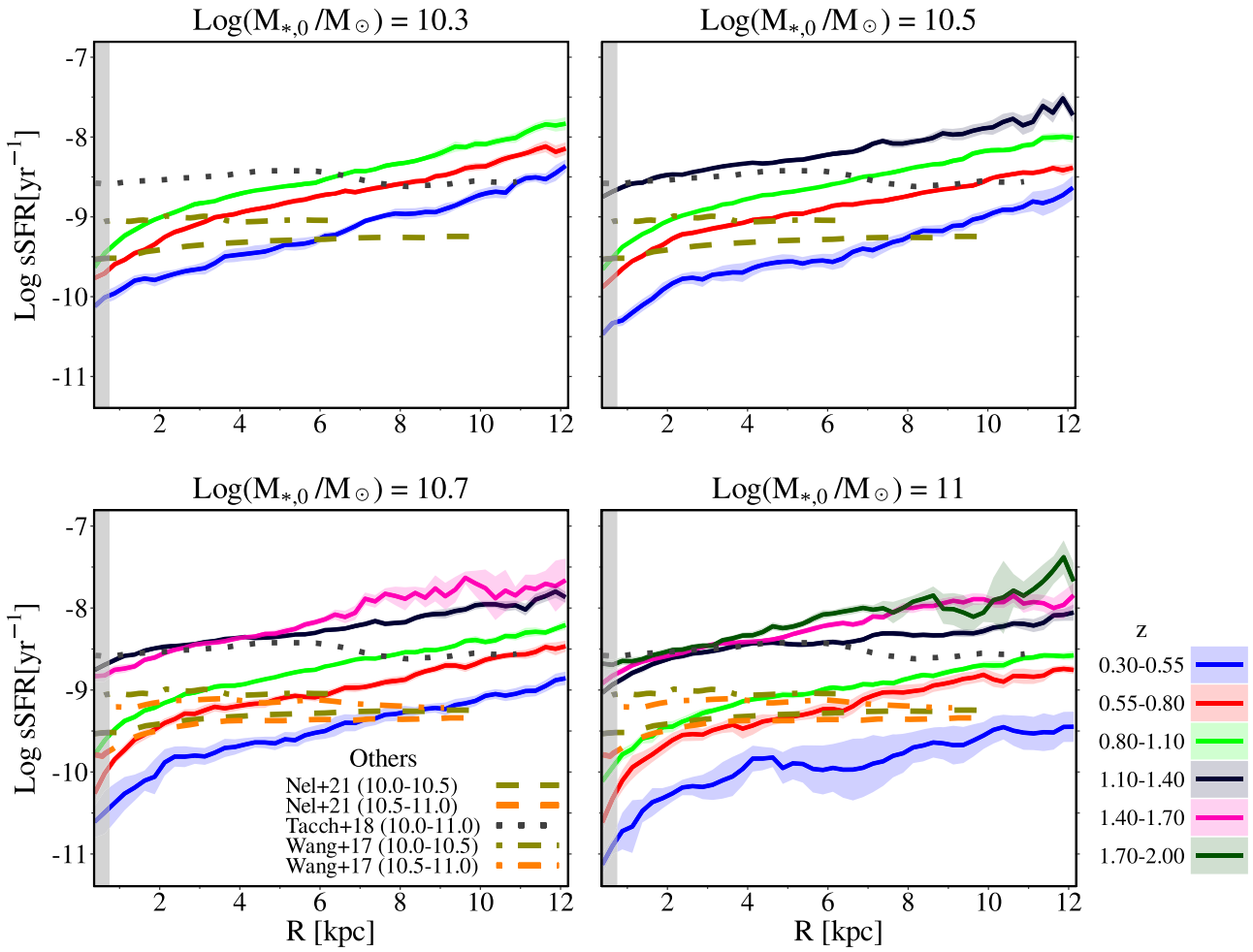

Figure 7. Comparison of our sSFR profiles (solid lines) with dust-corrected profiles measured by W. Wang et al. (2017; dashed–dotted lines) for SFGs in stellar mass ranges of $\log(M_*/M_\odot) = [10 - 10.5]$ (olive) and [10.5–11] (orange) at $1.0 < z < 1.2$ and by S. Tacchella et al. (2018; dotted gray lines) for star-forming MS galaxies with a stellar mass between 10^{10} and 10^{11} $M_\odot$ at $z \sim 2.2$. The dashed lines represent the sSFR profiles of galaxies with $\log(M_*/M_\odot) = [10.0, 10.5]$ (olive) and [10.5–11.0] (orange) at $z \sim 1.0$ from the TNG50 simulation derived by E. J. Nelson et al. (2021).

3.4. sSFR profiles

Using the resolved maps derived from the pixel-by-pixel SED fitting, we estimated the SFR and, accordingly, the sSFR profiles. Figure 7 shows the median sSFR profiles within the 12 kpc radius for six redshift bins. The shaded regions indicate bootstrapped scattering of the median SFR. These profiles show that the maximum SF activities occur at $z > 1.2$. While the sSFR decreases over time, the decline is faster in the inner regions compared to the outer parts until $z \sim 0.4$. It occurs more rapidly for high-mass galaxies, leading to shallower radial profiles at lower redshifts and higher masses.

In addition, it is interesting that higher-mass samples exhibit a centrally suppressed SF such that the sSFR in the central regions of SFGs with $\log(M_{*,0}/M_\odot) = 11$ attains the quenching threshold of 10^{-11} yr^{-1}. These observations are in line with the rapid growth of the Sérsic indices and Σ_1, indicating that in high-mass SFGs a central dense component (bulge or pseudobulge) with very low SFR has been formed and is growing. The mass-dependent SF activity in the central region of galaxies agrees with previous works (S. Tacchella et al. 2015, 2018; L. Morselli et al. 2019).

4. Discussion

In this section, we first compare our findings with those from previous simulations and observational studies and investigate the possible factors contributing to the variation in size growth rates. Then, we examine the evolution of the surface density of mass and SFR, as well as the spin parameter of the halo. Finally, we discuss the implications of our results on our understanding of the history of galaxy growth.

4.1. Comparison with Observational Studies

The distinctive aspect of this work is the selection of possible progenitors of galaxies and employing mass-based structural parameters. Due to these features, our results challenge some earlier findings stating that the sizes of SFGs increase considerably toward lower redshifts. In this section, we compare the circularized radii, r_{50}, of our samples with those of other observational studies. Figure 8 illustrates the circularized size evolution of galaxies inferred from Methods I and II, as well as those measured by previous studies (S. G. Patel et al. 2013a; C. Papovich et al. 2015; M. Mosleh et al. 2020; Z. Ji & M. Giavalisco 2023; T. B. Miller et al. 2023). The slope of the size growth rate depends on the stellar mass for both methods, although the obtained slope is shallower than previous estimates.

Our r_{50} measurements are consistent with the mass-based sizes of M. Mosleh et al. (2020; purple lines) and T. B. Miller et al. (2023; magenta lines), as can also be seen for effective

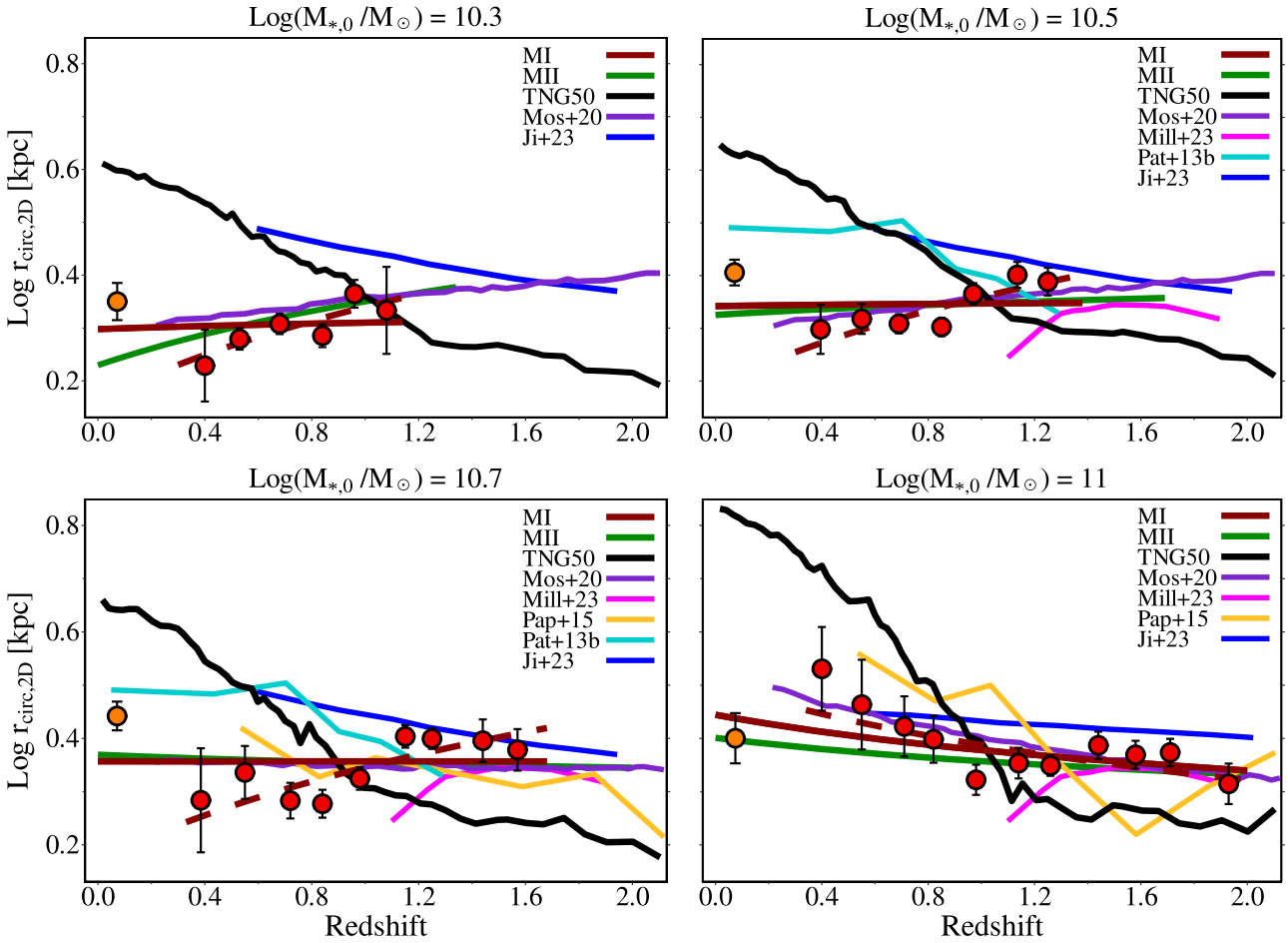

Figure 8. Comparison of the circularized size evolution of SFGs obtained from the first method with (dark-red lines) and without (orange lines) considering the $z \sim 0$ SDSS data with other works. It can be seen that the mass-based sizes of M. Mosleh et al. (2020; purple lines) and T. B. Miller et al. (2023; magenta lines) change very little, while the half-light radii of Z. Ji & M. Giavalisco (2023; blue lines), S. G. Patel et al. (2013a; cyan lines), and C. Papovich et al. (2015; orange lines) are often larger at lower redshifts.

radii in Figure 2. M. Mosleh et al. (2020) measured the mass-based structural parameters of galaxies in fixed stellar mass bins over the redshift range $z = 0.3$–2.0. Despite the same data, the slopes are slightly different because we identified the probable progenitors instead of the analysis at fixed mass. Our estimated size evolution trends are also in line with the slow size evolution of SFGs within the range of $10.5 < \log(M_*/M_\odot) < 11$ observed by T. B. Miller et al. (2023). They studied the evolution of the color gradient and half-mass radius of ∼3000 galaxies measured with the nonparametric framework of `imcascade` (T. B. Miller & P. van Dokkum 2021) in 3D-HST/CANDELS fields. This mild evolution is evident in other studies investigating the evolution of mass-based/NIR sizes along the semimajor axis (e.g., K. A. Suess et al. 2019b). Based on the JWST imaging, E. Ward et al. (2024) also reported a shallower rate of evolution at a fixed mass of $10^{10.7}$ $M_\odot$ (0.63 ± 0.07 for SFGs at $0.5 < z < 5$) compared to previous studies such as A. van der Wel et al. (2014).

Although C. Papovich et al. (2015) used optical sizes, their estimated trends for the progenitor-selected samples are compatible with our sizes within the redshift range of this study. However, despite using the same method (MSI), our estimated sizes differ more from the results of S. G. Patel et al. (2013a) compared to C. Papovich et al. (2015), who employed the abundance matching method. This could be attributed to the type of galaxies: S. G. Patel et al. (2013a) focused solely on SFGs, whereas C. Papovich et al. (2015) examined both SFGs and QGs. In addition, S. G. Patel et al. (2013a) assumed a constant M/L profile to convert light to mass profiles. Like C. Papovich et al. (2015), Z. Ji & M. Giavalisco (2023) utilized the sizes taken from the catalog of A. van der Wel et al. (2012) to analyze the size evolution of SFGs with $\log(M_*/M_\odot) = 10.3 - 10.8$ and $\log(M_*/M_\odot) > 10.8$ after eliminating the progenitor effect. Using the Prospector, they reconstructed the SFH of each galaxy to identify the probable progenitors with the same mass and SFR at the formation epoch. Their analysis revealed a much slower evolution for SFGs compared to C. Papovich et al. (2015), which can be partly attributed to separating the sample into SFGs and QGs.

A. Whitney et al. (2019) studied the evolution of Petrosian sizes measured by the nonparametric approach of concentration, asymmetry, and clumpiness (CAS; Conselice 2003) for two samples: a sample selected at the constant number density of $n = 1 \times 10^{-4}\,\mathrm{Mpc}^{-3}$ (corresponding to the present-day stellar mass of $\log(M_{*,0}/M_\odot) \sim 11.25$), and a sample at the fixed mass range of $\log(M_*/M_\odot) = 9.0 - 10.5$. The number-density-selected sample grows at a rate of -0.53 ± 0.16, which is in good agreement with the observed evolution of effective radius in our massive sample (-0.46 ± 0.12). The other sample (at fixed mass) revealed steeper slopes (-0.92 ± 0.03), supporting the idea that the rate of size evolution is faster in

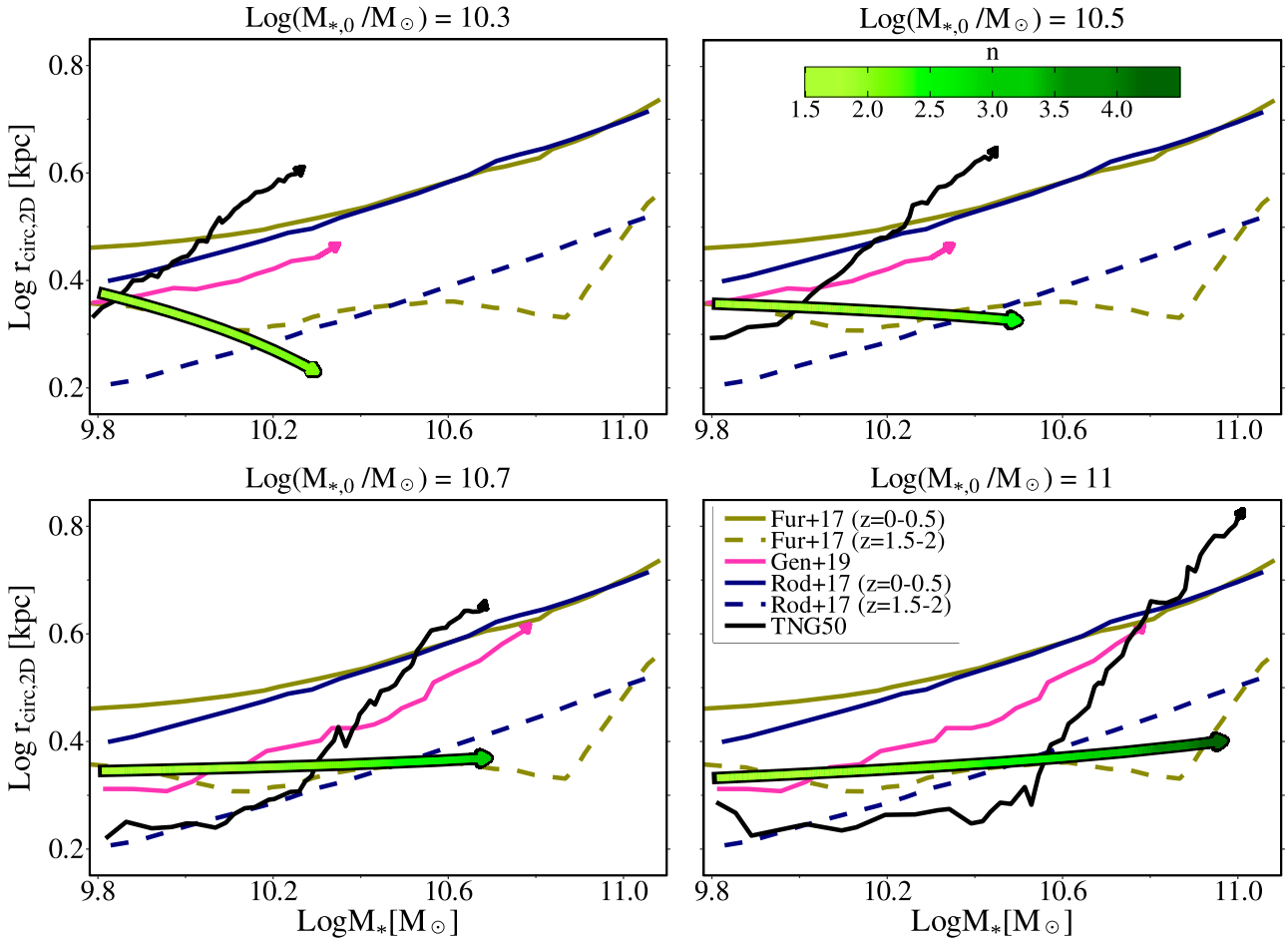

Figure 9. Half-mass radius–stellar mass evolutionary track of progenitors (thick green lines with arrows at the end) with four different final masses, color-coded to account for their Sérsic indices. We utilized the 2D circularized radii to compare our results with the simulations, including the evolutionary track of TNG100 (magenta lines) and the size–mass relation of Ref–*L*100*N*1504 EAGLE (olive lines) taken from S. Genel et al. (2018) and M. Furlong et al. (2017). In addition, we directly compared the sizes from observation with simulation by extracting the half-mass radius of galaxies selected from TNG50 (black lines) to calculate the SMGH. Generally, the growth rates predicted by the semiempirical model of A. Rodríguez-Puebla et al. (2017; navy lines) and simulations are faster than observations. This difference is even more significant if we compare the size growth predicted by TNG50 with that observed from selected SFGs with similar mass at each redshift.

the fixed-mass-selected samples relative to the progenitor-selected ones. In addition, our estimated slopes for the evolution of r_e are compatible with the measurements of A. George et al. (2024) for effective radii of SFGs at fixed mass, although they found a more rapid evolution in the size of samples with evolving mass at $0.1 < z < 0.9$. This disparity may arise from the methods used to calculate the mass growth and estimate the size. To measure the SMGH up to $z = 0.1$ for each galaxy with a specific mass at $z = 0.9$, they considered only SF without accounting for ML ($\Re$ in Equation (2)), resulting in much faster mass growth. In addition, the sizes of galaxies with a given mass were estimated from the size–mass relation they observed at each redshift.

4.2. Comparison with Simulations

Despite numerous attempts to reproduce the evolution of galaxies, the simulated sizes do not agree well with observations (C. Scannapieco et al. 2012; G. F. Snyder et al. 2017; W. J. Roper et al. 2022). While simulations like IllustrisTNG and EAGLE have made progress in reducing this difference by fine-tuning parameters like feedback and dust attenuation, their predictions remain inconsistent with observed measurements. As discussed in Section 1, simulations exhibit a considerable increase in the sizes of SFGs, whereas the observed half-mass radii do not change significantly. Therefore, we attempted to examine this disparity by comparing the size evolution of SFGs in the simulations with those observed. To carefully analyze the predicted sizes, the 3D half-mass radii (r_{3D}) of the simulations are converted to projected circularized sizes (r_{2D}) using the analytical relation of $r_{2D} = r_{3D}/1.3$, derived by G. van de Ven & A. van der Wel (2021).

In order to conduct a fair comparison with simulations, we extract the half-mass sizes of SFGs that we selected from TNG50-1 as the progenitors of each sample with a specific mass. The evolution of median sizes taken from TNG50-1 is shown as black lines in Figure 8. As can be seen, there is a notable disparity between the evolution of the projected half-mass sizes of TNG50 and our observations at $z < 0.8$. Furthermore, we directly compared the half-mass radius from the stellar mass tracks of Method II (thick green lines with arrows at the end color-coded to Sérsic indices) with those predicted by the TNG50-1 simulations (black lines with arrows) in Figure 9. As can be seen, there is a notable disparity between the projected half-mass sizes of TNG50 and our observations at later epochs. It should be noted that the evolutionary paths of progenitors chosen via Method I are similar to those obtained through Method II. Such a trend can

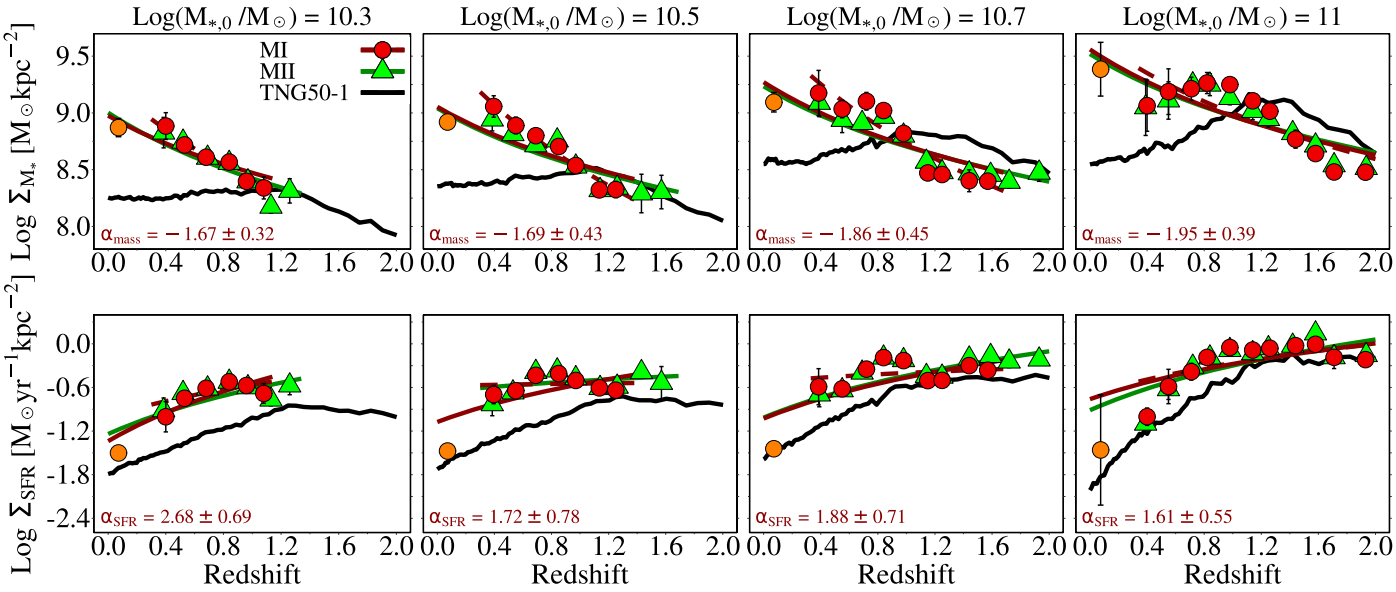

Figure 10. Stellar mass surface density, Σ_M (top panel), and SF surface density, $\Sigma_{\rm SFR}$ (bottom panel), of selected SFGs within the half-mass radius. $\Sigma_{\rm SFR}$ decreases toward low redshifts, in agreement with the TNG50 simulation (black lines) and previous observational works, whereas Σ_M increases from $z \sim 1.2$, in contrast to the simulation.

also be seen for the central and satellite progenitors in TNG100 measured by S. Genel et al. (2018). The evolutionary paths of these galaxies that remain star-forming at $z = 0$ with final mass ranges of $\log(M_{*,0}/M_\odot) = 10.3 - 10.45$ and 10.7–10.85 are shown by pink lines with arrows in Figure 9. To comprehend this trend, it is important to note that in the TNG simulations the local size–mass relations estimated from the light profiles (e.g., S. Shen et al. 2003) have been considered in order to discern between various simulated models.

For a more comprehensive analysis of this discrepancy, we use the size–mass relation of the EAGLE simulations, determined by M. Furlong et al. (2017), in two redshift intervals: 0.–0.5 (solid olive lines) and 1.5–2 (dashed olive lines). M. Furlong et al. (2017) examined the size evolution of active and passive galaxies from the EAGLE simulations over the range $0 < z < 2$ in two resolutions of 100 and 25 cMpc boxes: Ref–*L*100*N*1504, Ref–*L*025*N*0752, and Recal −*L*025*N*0752. While our evolutionary trajectories align with the predicted size–mass relations of the Ref−*L*100*N*1504 EAGLE simulation at $z = 1.5$–2, they diverge in the lowest redshift bin. Such dissimilarity between the simulations' half-mass sizes and observations was also reported by K. A. Suess et al. (2019b), M. Hasheminia et al. (2022), and T. B. Miller et al. (2023). It is worth noting that our results show relative consistency (particularly in the higher mass range) with Recal–*L*025*N*0752, which underwent recalibration for stellar feedback and AGN parameters in the 25 cMpc box. Nevertheless, the significant size growth in simulations is also inconsistent with the mild evolution of the observed mass-based sizes at $z < 1$ (K. A. Suess et al. 2019b; M. Mosleh et al. 2020; M. Hasheminia et al. 2022).

Finally, we analyze whether our findings align with the size–mass relation of a semiempirical model developed by A. Rodríguez-Puebla et al. (2017) in two redshift ranges of $0 < z < 0.5$ (solid navy lines) and $1.5 < z < 2$ (dashed navy lines). They utilized a semiempirical approach to establish a connection between galaxies and their host halos, allowing them to estimate the merger rates, SFHs, and structural parameters. To determine the size, they adopted the local size–mass relation of M. Mosleh et al. (2013) with the redshift-dependent coefficients constrained by the size–mass evolution of A. van der Wel et al. (2014). As evident from Figure 9, the evolution of their size–mass relation proposes a size growth with a steeper slope compared to our results. Adopting the mass–size relation of the local galaxies based on their light profiles can be one of the origins of the discrepancies.

Differences in the size evolution rates can be reflected in quantities such as the surface density of stellar mass (Σ_M) and SFR ($\Sigma_{\rm SFR}$). Therefore, we compare the Σ_M and $\Sigma_{\rm SFR}$ of our samples with those predicted by TNG50 (black lines) in Figure 10. The stellar mass surface density is defined as a function of the half-mass radius by

$$\Sigma_M = \frac{M_*}{2\pi r_{50}^2}. \quad (6)$$

The same approach is used to calculate SFR density.

In general, the stellar mass surface densities of our observed samples tend to rise. More massive galaxies exhibit higher stellar mass surface density: for samples with $\log(M_{*,0}/M_\odot) = 10.3$ and 11, the median Σ_M values in the local Universe reach $10^{8.9}$ and $10^{9.4}$ $M_\odot$ kpc^{-2}, respectively. It seems that the mass surface density of massive galaxies reaches the highest value around $\log(\Sigma_M) \sim 9.2$ and then remains relatively constant, but the lower-mass SFGs keep building the stellar mass inside the effective radius. Although TNG50 SFGs show a similar mass dependence, their surface densities demonstrate a decreasing pattern at $z < 1$. As Method II relies on TNG50's SMGHs for sample selection, this distinction between our results and TNG50 possibly arises from the notable growth of the half-mass radii in simulations since $z \sim 1$. This rapid expansion indicates the necessity of some mechanisms in simulation to regulate the size growth.

As shown in the bottom panel of Figure 10, the SFR surface densities obtained from Methods I and II are almost identical, indicating an overall decline in the $\Sigma_{\rm SFR}$, especially at $z \sim 0.8$. Our samples at $z > 0.6$ show a positive relation between their

stellar mass and $\Sigma_{\rm SFR}$, i.e., more massive SFGs tend to have a higher $\Sigma_{\rm SFR}$ value. Our observational trends align with previous works (Y. Ono et al. 2013; T. Shibuya et al. 2015, 2019; T. Morishita et al. 2024). In addition, the findings of T. Morishita et al. (2024) provided evidence that supports the correlation between SFR and the stellar mass of galaxies, while T. Shibuya et al. (2015) presented a contradictory conclusion. However, the values we obtained are within the range $-1.5 < \log(\Sigma_{\rm SFR}) < 0.15$, as derived by T. Shibuya et al. (2015). Hence, the distinct conclusion reached by T. Shibuya et al. (2015) can be ascribed to selecting samples in fixed mass bins.

The SFR surface densities of TNG50 (black lines) are almost parallel to our findings, due to the slower decline in their SF activities. As seen in Figure 1, the assembled mass is nearly equal, while the SFR in TNG50 is lower than in our measurements. Hence, it can be inferred that the contribution of other channels, such as merger and accretion, to the stellar mass accumulation is higher in TNG simulations compared to observations. Moreover, the decline in surface density of SFR could be related to the dynamical effects. According to the simple model of M. D. Lehnert et al. (2015) for sSFR evolution, increasing the angular momentum (AM) of the accreted gas toward lower redshifts can lead to a reduction in both the surface density of the gas and SFR. The model predicts that the high AM causes the transfer of accreted gas to larger radii and the accumulation of mass in the disk's outer regions, consequently leading to an expansion in size. Therefore, the decreasing trend of SFR surface density evolution and significant size growth in the simulation may be attributed to the high AM of accreted gas, as suggested by this model.

To get more insights into the origins of dissimilarity in sizes, we discuss the following contributed mechanisms:

1. *Feedback and Radial Gradient of M/L Ratio*. The impact of feedback mechanisms on the efficiency of SF and scaling relations was examined by many studies (A. A. Dutton & F. C. van den Bosch 2009; M. Aumer et al. 2013; F. Shankar et al. 2013; M. Noguchi 2018). A. A. Dutton & F. C. van den Bosch (2009), for example, used a disk galaxy evolution model. It has been found that feedback can lead to a shallower slope in the size–mass relation of galaxies. Thus, considering the relative agreement between Recal–*L*025*N*0752 and the observational data, as well as the findings of previous studies such as A. A. Dutton & F. C. van den Bosch (2009), we emphasize that fine-tuning the feedback can enhance the consistency between observed and simulated sizes, as suggested by K. A. Suess et al. (2019b). In addition, disagreement in sizes can also be attributed to dissimilarity in M/L ratios between simulations and observations. The little disparity between the growth rates of the half-mass and half-light radii in different simulations indicates that the distribution of mass and light is relatively consistent in simulations. Moreover, it is evident from Figures 2 and 3 in S. Genel et al. (2018) that the $r_{e,\rm mass}/r_{e,\rm light}$ in TNG100 is larger than the observed ratios (M. Mosleh et al. 2017, 2020; K. A. Suess et al. 2019a; T. B. Miller et al. 2023; A. van der Wel et al. 2024). Thus, it can be concluded that the M/L in TNG100 is higher than the observed ratio obtained by M. Mosleh et al. (2017) and K. A. Suess et al. (2019a). One explanation for this difference could be the calibration of M/L using local observables in simulations, without accounting for the color gradient's evolution with redshift, especially at $z < 1.5$. However, for a more thorough investigation, it is crucial to measure the M/L or color gradient in simulations and compare it with the findings from observational studies.
2. *Redistribution of stellar mass*. Besides the mentioned possibilities, the dynamical effects can also change the stellar mass distribution in galaxies. Hence, comparing the dynamical evolution of SFGs in simulation and observation can help to clarify the impact of this factor on the size discrepancy. In the following, we investigate the redshift variation of AM in TNG simulations as a proxy for dynamical changes and compare it with our findings. We analyze the evolution of "galaxy spin," $\lambda_{\rm gal} = \lambda_{\rm halo}\,(j_d/m_d)$, using the simple disk formation models (S. M. Fall & G. Efstathiou 1980; S. M. Fall 1983; H. J. Mo et al. 1998). According to these models, baryons settled in disks will have a mass and AM that are a relatively constant fraction of the mass (m_d) and AM (j_d) of their host dark matter halo. These models predict that the disk scale length is a fixed fraction of the halo size given by

$$R_{\rm gal} = \frac{\lambda_{\rm halo}}{\sqrt{2}}\left(\frac{j_d}{m_d}\right)R_{\rm halo}, \tag{7}$$

where

$$R_{\rm halo} = \left(\frac{GM_{\rm halo}}{100H^2(z)}\right)^{1/3} = \frac{V_{\rm halo}}{10H(z)}. \tag{8}$$

Here $\lambda_{\rm halo}$ and $H(z)$ are the halo spin and the Hubble parameter at a given redshift z, respectively. Therefore, the size of the disk evolves as $(1+z)^{-1}$ at a constant halo mass, while at constant circular velocity it grows even faster with $(1+z)^{-1.5}$. By substituting Equation (8) into Equation (7), with $E = -M_{\rm halo}V_c^2/2$ and $r_e = 1.68R_{\rm gal}$, the galaxy spin could be related to the halo mass and effective radius of a disk galaxy via

$$r_e \simeq 0.26\lambda_{\rm halo}\left(\frac{j_d}{m_d}\right)\left(\frac{GM_{\rm halo}}{H(z)^2}\right)^{1/3}. \tag{9}$$

By comparing the size in the first redshift bin to that in the last redshift bin, the stability of galaxy spin over time can be estimated as

$$\frac{\lambda_{\rm gal,0}}{\lambda_{\rm gal,z}} = \left(\frac{M_{\rm halo,z}}{M_{\rm halo,0}}\right)^{1/3}\left(\frac{H(0)}{H(z)}\right)^{2/3}\frac{r_{e,0}}{r_{e,z}}. \tag{10}$$

By extracting the corresponding halo mass of each stellar mass from TNG50 and calculating the changes in the size of SFGs selected by Method II, we find that observed galaxies with $\log(M_{*,0}/M_\odot) = 10.3$, 10.5, 10.7, and 11 have $\frac{\lambda_{\rm gal,0}}{\lambda_{\rm gal,z}} = 0.47$, 0.68, 0.59, and 0.46 since $z = 1.38$, 1.75, 2, and 2, respectively. If the halo spin parameter remains constant over the redshift range of this study, our samples now possess around half their initial retention fraction of specific AM (sAM), j_d/m_d. By assuming that the initial sAM of the baryons and that of the dark matter are the same, the average fraction of AM retained in the disk from the halo is close to 55% within the past 10 Gyr. This is in good agreement with the retained fraction of

0.63 ± 0.06 found by Romeo et al. (2023) for the stellar content of nearby SFGs. In addition, our results are relatively consistent with those measured by A. M. Swinbank et al. (2017), who found that rotationally supported galaxies with $V/\sigma > 5$ retain ~70% of their dark matter sAM. Their investigation revealed that galaxies with a higher ratio of $V/\sigma > 5$ tend to have higher sAM, lower SFR surface density, more pronounced bulges, and smoother disks at fixed mass. Furthermore, A. Burkert et al. (2016) conducted a study on the Hα integral field unit kinematics of 359 SFGs at $z \sim 0.8$–2.6 and a stellar mass range of $\log(M_*/M_\odot) \sim 9.3 - 11.8$. They concluded that for SFGs 60%–90% of the sAM of their halo transferred to baryonic disk since $z = 2.6$.

According to the sizes extracted from TNG50, the simulations predict higher values of 1.11, 0.97, 0.94, and 1.30 for corresponding SFGs. Since m_d in simulation and observation are relatively similar, we can define the retention fraction of sAM as the AM fraction of the disk to its host halo. Assuming a constant $\lambda_{\rm halo}$ suggests that the fraction of AMs in the simulated galaxies is relatively stable, while observations demonstrate a substantial reduction in this ratio. This stability in the retention fraction of AM of simulated SFGs, which results in the redistribution of stellar mass and subsequent growth in size, could be attributed to the high efficiency of AM transfer from the accreted halo gas to the disks in simulations.

4.3. Implications for the Evolution of SFGs

Our results show that how the mass assembles at different radii depends on the galaxy's stellar mass: within the redshift range of this study, for SFGs with $\log(M_{*,0}/M_\odot) = 10.3$, the interior regions assemble relatively faster, while the outskirts of massive galaxies ($\log(M_{*,0}/M_\odot) = 11$) are undergoing much higher rates of mass growth than the inner parts. We can also see this trend reflected in the evolution of the r_{20} and r_{80} sizes, so that for the r_{20} size the slope of the evolution becomes shallower with increasing mass, while the growth rate of r_{80} increases. In addition, Σ_M, Σ_1, and Sérsic index of SFGs are also correlated with their mass, so galaxies with higher mass tend to have higher mass surface density, a more compact central component, and a prominent bulge.

However, the analysis of samples with $\log(M_{*,0}/M_\odot) \sim 10.5 - 10.7$ reveals that the mass growth rates are nearly comparable across all radii. This finding supports the notion that mass accumulates self-similarly in this mass regime, which is aligned with a lack of significant changes in the half-mass size of these SFGs. The modest evolution in size, accompanied by the considerable increase in mass, causes the surface density of these galaxies to rise constantly, reaching around $10^9\ M_\odot\ {\rm kpc}^{-2}$ in the local Universe.

These results suggest that massive galaxies are undergoing a different evolutionary stage. Over the redshift range of $1.2 < z < 2.0$, the inner parts experience only three times increase in mass, while the mass in the outer regions increases by a factor of 12. Following a period of spatially consistent mass buildup, the growth rate in the outskirts rises again since $z \sim 0.7$, contrasting with a slow mass accumulation rate in the inner regions. During this epoch, the growth of Σ_M and Σ_1 slows down, with the central surface density surpassing the median value of QGs. It can be interpreted as the initial stage of mass saturation (S. Tacchella et al. 2015; C. Abdurro'uf et al. 2023; S. Lapiner et al. 2023) in the interiors of massive SFGs. In addition, although all samples show a common trend of rising sSFR profiles, the decline in sSFR is more pronounced in the inner regions of massive galaxies. The sSFR in their central 1 kpc region drops from $10^{-8.8}\ {\rm yr}^{-1}$ at $1.20 < z < 1.35$ to the quenching threshold $10^{-11}\ {\rm yr}^{-1}$ at $0.45 < z < 0.60$, indicating the inside-out quenching. These findings support the idea that the SF activities of galaxies cease when their central density reaches a critical value (J. J. Fang et al. 2013; G. Barro et al. 2017; K. E. Whitaker et al. 2017).

Recent studies suggested that when halos reach a critical mass ($M_{\rm shock}$) they establish stable shocks that can heat the infalling gas to near the virial temperature, causing a hot circumgalactic medium. The cold streams cannot penetrate through this medium at $z < z_{\rm crit}$, leading to the suppression of gas supply and, therefore, long-term quenching (Y. Birnboim & A. Dekel 2003; D. Kereš et al. 2005; A. Dekel & Y. Birnboim 2006; S. Tacchella et al. 2016; P. Behroozi et al. 2019). At $z < 1$, the halo mass of our massive sample surpasses the critical mass, suggesting that these galaxies may experience long-term quenching, as cold flows have been halted since $z \sim 2$.

Although at $z < 1$ the massive SFGs have lower sSFR in outer regions compared to other samples, their sizes exhibit more rapid growth. A possible explanation could be the accretion or merger events, which have been found to play an essential role in the size and mass growth of massive SFGs at lower redshifts (V. Rodriguez-Gomez et al. 2016; A. Pillepich et al. 2018; M. Mosleh et al. 2020; L. Kawinwanichakij et al. 2021).

4.4. Robustness of the Size Estimation

Obtaining the half-mass sizes depends on the methods for converting the images to mass distribution and then measuring the structural parameters from these maps. These processes involve many assumptions, as well as diverse methods of size measurement, and consequently cause uncertainties. Therefore, we briefly discuss the impacts of these factors in this section.

The complexities involved in estimating the distribution of stellar mass within galaxies make it challenging to calculate the stellar-mass-weighted parameters. Due to these difficulties, various methods have been employed to derive the mass profiles. In previous studies, the estimation of stellar mass information has relied on either SED fitting (M. Mosleh et al. 2017; K. A. Suess et al. 2019a; M. Mosleh et al. 2020) or color–M/L relations (K. A. Suess et al. 2019a; T. B. Miller et al. 2023; A. van der Wel et al. 2024). In addition, the mass profiles can be estimated directly from the 1D light profiles (M. Mosleh et al. 2017; K. A. Suess et al. 2019a; T. B. Miller et al. 2023; A. van der Wel et al. 2024) or by creating 2D mass maps and finding the best-fit 1D profiles (K. A. Suess et al. 2019a; M. Mosleh et al. 2020). Employing diverse approaches, in combination with the uncertainties in SED fitting or measuring the color–M/L relationships, has the potential to introduce variation in the estimated mass-based sizes. Despite a few reported discrepancies that need more careful investigation (e.g., A. van der Wel et al. 2024), it is interesting that there is an overall consistency among most studies regarding the evolution of half-mass size (M. Mosleh et al. 2017, 2020; K. A. Suess et al. 2019a, 2019b; M. Hasheminia et al. 2022;

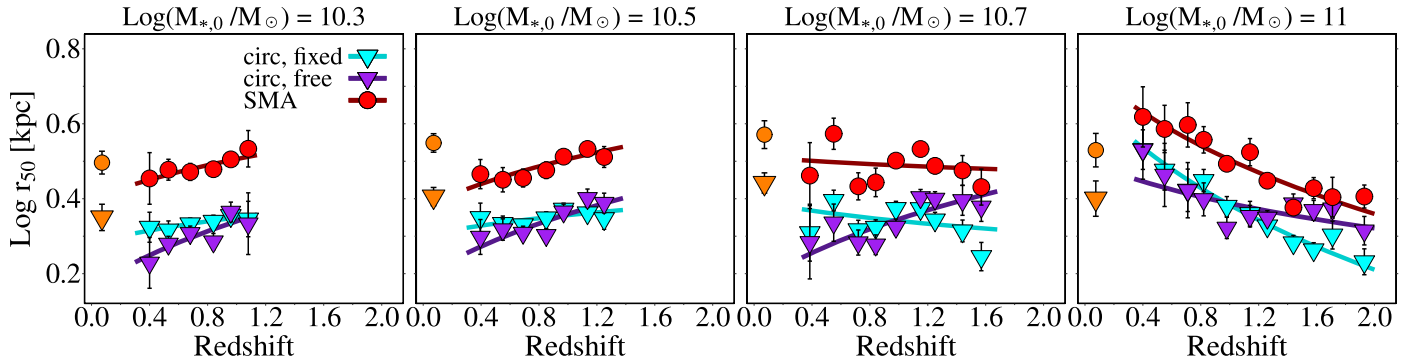

Figure 11. Comparing the redshift evolution of half-mass radius along the semimajor axis $r_{\rm SMA}$ (red circles) with circularized half-mass size estimated from averaged b/a of galaxy $r_{\rm circ,fixed}$ (cyan downward-pointing triangles) and circularized mass profiles fitting with free b/a and PA at each radius $r_{\rm circ,free}$ (purple downward-pointing triangles) derived by M. Mosleh et al. (2020). Although $r_{\rm SMA}$ is larger than $r_{\rm circ}$ and the median best-fit slopes are slightly different in some mass, there is no significant evolution in the half-mass sizes.

T. B. Miller et al. 2023). For instance, our results are robust by using mass-based sizes from K. A. Suess et al. (2019a). Therefore, it can be concluded that the discrepancy in the evolution of half-mass sizes compared to the light-based sizes cannot be attributed to uncertainties in observations.

In addition, circularized sizes are frequently used in the literature. To ensure that the results are independent of size definition and methodology, we compared the evolution of the circularized half-mass radii with growth from semimajor-axis sizes. In our analysis, two methods can be used to circularize the radius: one way is to fit fixed-center ellipses to the galaxy's isophotes or isomasses, while PAs and ellipticities (e) are free parameters. The profiles can be circularized at each radius using the corresponding axis ratio (b/a). Thus, the circularized mass- or light-weighted size is determined locally by fitting ellipses with free parameters ($r_{\rm circ,free}$).

The size of the galaxy can also be circularized based on its average axis ratio $(b/a)_{\rm avg}$: $r_{\rm circ,fixed} = r_{\rm SMA}\sqrt{(b/a)_{\rm avg}}$. We define $(b/a)_{\rm avg}$ as the average of axis ratio profiles in the range of $2r_{e,\rm SMA}$ to the radius at which the stellar mass surface density reaches $10^7\ M_\odot\,{\rm kpc}^{-2}$. Due to the differences in the axis ratio of inner and outer regions, the circularized half-mass radii obtained from these two methods shows some differences. As shown in Figure 11, even though the $r_{e,\rm SMA}$ is relatively larger, the slope of its redshift evolution is roughly in line with that of the circularized radii, particularly $r_{\rm circ,fixed}$. Hence, the general evolution of the mass-based sizes is not affected by the way the sizes are estimated.

Finally, given the discrepancy in the evolutionary paths of observational light- and mass-based radii, more detailed and comprehensive studies are required to measure the size growth rates of galaxies and explore the underlying factors contributing to these differences in the literature. The high spatial resolution and NIR coverage of the James Webb Space Telescope (JWST) will allow us to measure mass-based structural parameters more precisely at higher redshifts and lower mass regimes. Additionally, it is crucial to undertake more precise analyses to identify the parameters that influence the more rapid evolution of the half-mass radii in the simulations compared to those estimated from observations. A simultaneous investigation of the color gradients and SFR profiles with advanced observational tools like the JWST can provide valuable insights into the complex mechanisms underlying the structural evolution of galaxies. Furthermore, combining these observations with state-of-the-art simulations will help us understand the existing discrepancies in the size evolution of simulated and observed galaxies.

5. Summary

By analyzing the structural evolution and SF activity of SFGs with a present-day stellar mass of $\log(M_{*,0}/M_\odot) = 10.3 - 11.0$, this study sheds light on the radial accumulation of stellar mass and the mechanisms that govern the assembly of different components since cosmic noon. In order to reduce biases resulting from employed methods for sample selection and parameter measurement, we attempted to track the structural evolution of each individual galaxy by utilizing parameters derived from the stellar mass maps. Our approach involves calculating the SMGH of SFGs with a given mass, followed by the identification of potential progenitors through Method I to reconstruct its evolutionary path. In addition, we have utilized the average SMGHs from the TNG50 simulations to corroborate our findings and directly compare them with simulations. The results indicate that there is no significant difference between the SMGHs calculated by these methods within the mass and redshift ranges of this study. Our key findings are summarized as follows:

1. In the case of intermediate-to-high-mass progenitors, the evolution of mass-weighted sizes exhibits shallower slopes compared to light-weighted sizes, underscoring the crucial role of color gradients in the analysis of galaxy evolution.
2. Our results reveal that the evolution of SFGs depends on their final stellar mass. For intermediate- and lower-mass SFGs ($\log(M_{*,0}/M_\odot) < 10.8$), the sizes of r_{50} and r_{80} remain almost unchanged over the past 10 Gyr, whereas r_{20} tends to decrease, implying an increase in the concentration of the stellar mass distribution. On the other hand, at the massive end ($\log(M_{*,0}/M_\odot) > 10.8$), these two radii increase with cosmic time, leading to the r_{50} and r_{80} size evolution rates of $(1+z)^{-0.46\pm0.12}$ and $(1+z)^{-0.99\pm0.21}$, respectively.
3. The high-mass sample exhibits an inside-out growth pattern, whereas the intermediate- and lower-mass SFGs accumulate their mass in a relatively self-similar manner.
4. Even with similar SMGHs, the observed rates of size evolution differ from the predictions made by TNG50 simulations. The variations in feedback mechanisms,

radial M/L gradient, or mass redistribution may explain these differences.

5. Our calculations, based on r_e and halo mass from TNG50, reveal that the AM remains relatively unchanged in simulations while the observed AM experiences a significant reduction since $z \sim 2$, which may result from the accretion of high-AM gas in the simulations.

Overall, our results highlight the complexity of galaxy structural evolution and the necessity of accurately measuring size growth rates to understand the differences between the observed light- and mass-based radii, as well as the faster size evolution in simulations.

Acknowledgments

We thank the anonymous referee for the thorough review and valuable comments, which improved this manuscript. This work is based on observations taken by the 3D-HST Treasury Program (GO 12177 and 12328) with the NASA/ESA HST, which is operated by the Association of Universities for Research in Astronomy, Inc., under NASA contract NAS5-26555.

Facility: HST, Sloan.

Software: GALFIT (C. Y. Peng et al. 2010), ggplot2 (H. Wickham 2016), IRAF (D. Tody 1986, 1993), iSEDfit (J. Moustakas et al. 2013), R (R Core Team 2021), tidyverse (H. Wickham et al. 2019).

ORCID iDs

Maryam Hasheminia https://orcid.org/0000-0003-3428-6441
Moein Mosleh https://orcid.org/0000-0002-4111-2266
S. Zahra Hosseini-ShahiSavandi https://orcid.org/0000-0003-3449-2288
Sandro Tacchella https://orcid.org/0000-0002-8224-4505

References

Abazajian, K. N., Adelman-McCarthy, J. K., Agüeros, M. A., et al. 2009, ApJS, 182, 543
Abdurro'uf, Coe, D., Jung, I., et al. 2023, ApJ, 945, 117
Allen, R. J., Kacprzak, G. G., Glazebrook, K., et al. 2017, ApJL, 834, L11
Aumer, M., White, S. D. M., Naab, T., et al. 2013, MNRAS, 434, 3142
Barden, M., Rix, H.-W., Somerville, R. S., et al. 2005, ApJ, 635, 959
Barro, G., Faber, S. M., Koo, D. C., et al. 2017, ApJ, 840, 47
Behroozi, P., Wechsler, R. H., Hearin, A. P., et al. 2019, MNRAS, 488, 3143
Birnboim, Y., & Dekel, A. 2003, MNRAS, 345, 349
Bournaud, F., Elmegreen, B. G., & Elmegreen, D. M. 2007, ApJ, 670, 237
Bouwens, R. J., Illingworth, G. D., Blakeslee, J. P., et al. 2004, ApJL, 611, L1
Brammer, G. B., van Dokkum, P. G., Franx, M., et al. 2012, ApJS, 200, 13
Bruce, V. A., Dunlop, J. S., McLure, R. J., et al. 2014, MNRAS, 444, 1660
Buitrago, F., Trujillo, I., Conselice, C. J., et al. 2008, ApJL, 687, L61
Burkert, A., Förster Schreiber, N. M., Genzel, R., et al. 2016, ApJ, 826, 214
Chabrier, G. 2003, PASP, 115, 763
Chan, J. C. C., Beifiori, A., Mendel, J. T., et al. 2016, MNRAS, 458, 3181
Conselice, C. J. 2003, ApJS, 147, 1
Curtis-Lake, E., McLure, R. J., Dunlop, J. S., et al. 2016, MNRAS, 457, 440
Dahlen, T., Mobasher, B., Dickinson, M., et al. 2007, ApJ, 654, 172
Dekel, A., & Birnboim, Y. 2006, MNRAS, 368, 2
Dekel, A., Sari, R., & Ceverino, D. 2009, ApJ, 703, 785
Donnari, M., Pillepich, A., Nelson, D., et al. 2019, MNRAS, 485, 4817
Du, M., Ho, L. C., Debattista, V. P., et al. 2020, ApJ, 895, 139
Dutton, A. A., & van den Bosch, F. C. 2009, MNRAS, 396, 141
Engler, C., Pillepich, A., Joshi, G. D., et al. 2021, MNRAS, 500, 3957
Faisst, A. L., Carollo, C. M., Capak, P. L., et al. 2017, ApJ, 839, 71
Fall, S. M. 1983, in IAU Symp. 100 Internal Kinematics and Dynamics of Galaxies, ed. E. Athanassoula (Cambridge: Cambridge Univ. Press), 391
Fall, S. M., & Efstathiou, G. 1980, MNRAS, 193, 189
Fang, J. J., Faber, S. M., Koo, D. C., et al. 2013, ApJ, 776, 63
Ferguson, H. C., Dickinson, M., Giavalisco, M., et al. 2004, ApJL, 600, L107
Franx, M., van Dokkum, P. G., Förster Schreiber, N. M., et al. 2008, ApJ, 688, 770
Furlong, M., Bower, R. G., Crain, R. A., et al. 2017, MNRAS, 465, 722
Genel, S., Nelson, D., Pillepich, A., et al. 2018, MNRAS, 474, 3976
Genzel, R., Burkert, A., Bouché, N., et al. 2008, ApJ, 687, 59
George, A., Damjanov, I., Sawicki, M., et al. 2024, MNRAS, 528, 4797
Gómez-Guijarro, C., Elbaz, D., Xiao, M., et al. 2022, A&A, 658, A43
Graham, A. W., & Worley, C. C. 2008, MNRAS, 388, 1708
Grogin, N. A., Kocevski, D. D., Faber, S. M., et al. 2011, ApJS, 197, 35
Hasheminia, M., Mosleh, M., Tacchella, S., et al. 2022, ApJL, 932, L23
Hathi, N. P., Malhotra, S., & Rhoads, J. E. 2008, ApJ, 673, 686
Hill, A. R., Muzzin, A., Franx, M., et al. 2017, ApJ, 837, 147
Hilz, M., Naab, T., & Ostriker, J. P. 2013, MNRAS, 429, 2924
Holwerda, B. W., Bouwens, R., Oesch, P., et al. 2015, ApJ, 808, 6
Huang, K.-H., Ferguson, H. C., Ravindranath, S., et al. 2013, ApJ, 765, 68
Ibarra-Medel, H., Avila-Reese, V., Lacerna, I., et al. 2022, MNRAS, 510, 5676
Jedrzejewski, R. I. 1987, MNRAS, 226, 747
Ji, Z., & Giavalisco, M. 2023, ApJ, 943, 54
Jiménez-Andrade, E. F., Magnelli, B., Karim, A., et al. 2019, A&A, 625, A114
Jiménez-Andrade, E. F., Murphy, E. J., Heywood, I., et al. 2021, ApJ, 910, 106
Kauffmann, G., White, S. D. M., Heckman, T. M., et al. 2004, MNRAS, 353, 713
Kawamata, R., Ishigaki, M., Shimasaku, K., et al. 2018, ApJ, 855, 4
Kawinwanichakij, L., Silverman, J. D., Ding, X., et al. 2021, ApJ, 921, 38
Kelvin, L. S., Driver, S. P., Robotham, A. S. G., et al. 2012, MNRAS, 421, 1007
Kereš, D., Katz, N., Weinberg, D. H., et al. 2005, MNRAS, 363, 2
Koekemoer, A. M., Faber, S. M., Ferguson, H. C., et al. 2011, ApJS, 197, 36
Kormendy, J., & Kennicutt, R. C. 2004, ARA&A, 42, 603
Krumholz, M. R., & Dekel, A. 2010, MNRAS, 406, 112
La Barbera, F., De Carvalho, R. R., De La Rosa, I. G., et al. 2010, MNRAS, 408, 1313
Lange, R., Driver, S. P., Robotham, A. S. G., et al. 2015, MNRAS, 447, 2603
Lapiner, S., Dekel, A., Freundlich, J., et al. 2023, MNRAS, 522, 4515
Lehnert, M. D., van Driel, W., Le Tiran, L., et al. 2015, A&A, 577, A112
Leitner, S. N., & Kravtsov, A. V. 2011, ApJ, 734, 48
Lindroos, L., Knudsen, K. K., Stanley, F., et al. 2018, MNRAS, 476, 3544
Liu, C., Mutch, S. J., Poole, G. B., et al. 2017, MNRAS, 465, 3134
Maltby, D. T., Almaini, O., Wild, V., et al. 2018, MNRAS, 480, 381
Marshall, M. A., Mutch, S. J., Qin, Y., et al. 2019, MNRAS, 488, 1941
Miller, T. B., & van Dokkum, P. 2021, ApJ, 923, 124
Miller, T. B., van Dokkum, P., & Mowla, L. 2023, ApJ, 945, 155
Miller, T. B., van Dokkum, P., Mowla, L., et al. 2019, ApJL, 872, L14
Mo, H. J., Mao, S., & White, S. D. M. 1998, MNRAS, 295, 319
Möllenhoff, C., Popescu, C. C., & Tuffs, R. J. 2006, A&A, 456, 941
Momcheva, I. G., Brammer, G. B., van Dokkum, P. G., et al. 2016, ApJS, 225, 27
Morishita, T., Ichikawa, T., & Kajisawa, M. 2014, ApJ, 785, 18
Morishita, T., Stiavelli, M., Chary, R.-R., et al. 2024, ApJ, 963, 9
Morselli, L., Popesso, P., Cibinel, A., et al. 2019, A&A, 626, A61
Mosleh, M., Hosseinnejad, S., Hosseini-ShahiSavandi, S. Z., et al. 2020, ApJ, 905, 170
Mosleh, M., Tacchella, S., Renzini, A., et al. 2017, ApJ, 837, 2
Mosleh, M., Williams, R. J., & Franx, M. 2013, ApJ, 777, 117
Mosleh, M., Williams, R. J., Franx, M., et al. 2011, ApJ, 727, 5
Mosleh, M., Williams, R. J., Franx, M., et al. 2012, ApJL, 756, L12
Moustakas, J., Coil, A. L., Aird, J., et al. 2013, ApJ, 767, 50
Mowla, L. A., van Dokkum, P., Brammer, G. B., et al. 2019, ApJ, 880, 57
Nelson, D., Pillepich, A., Springel, V., et al. 2019, MNRAS, 490, 3234
Nelson, E. J., Tacchella, S., Diemer, B., et al. 2021, MNRAS, 508, 219
Nelson, E. J., van Dokkum, P. G., Förster Schreiber, N. M., et al. 2016, ApJ, 828, 27
Noguchi, M. 1999, ApJ, 514, 77
Noguchi, M. 2018, ApJ, 853, 67
Oesch, P. A., Bouwens, R. J., Carollo, C. M., et al. 2010, ApJL, 709, L21
Ono, Y., Ouchi, M., Curtis-Lake, E., et al. 2013, ApJ, 777, 155
Ormerod, K., Conselice, C. J., Adams, N. J., et al. 2024, MNRAS, 527, 6110
Papovich, C., Labbé, I., Quadri, R., et al. 2015, ApJ, 803, 26
Patel, S. G., Fumagalli, M., Franx, M., et al. 2013a, ApJ, 778, 115
Patel, S. G., van Dokkum, P. G., Franx, M., et al. 2013b, ApJ, 766, 15
Paulino-Afonso, A., Sobral, D., Buitrago, F., et al. 2017, MNRAS, 465, 2717
Peletier, R. F., & Balcells, M. 1996, AJ, 111, 2238
Peng, C. Y., Ho, L. C., Impey, C. D., et al. 2010, AJ, 139, 2097
Pierini, D., Maraston, C., Bender, R., et al. 2004, MNRAS, 347, 1

Pillepich, A., Nelson, D., Hernquist, L., et al. 2018, MNRAS, 475, 648
Pillepich, A., Nelson, D., Springel, V., et al. 2019, MNRAS, 490, 3196
R Core Team, 2021 R: A Language and Environment for Statistical Computing, R Foundation for Statistical Computing, https://www.R-project.org/
Renzini, A. 2009, MNRAS, 398, L58
Rodriguez-Gomez, V., Genel, S., Vogelsberger, M., et al. 2015, MNRAS, 449, 49
Rodriguez-Gomez, V., Pillepich, A., Sales, L. V., et al. 2016, MNRAS, 458, 2371
Rodríguez-Puebla, A., Primack, J. R., Avila-Reese, V., et al. 2017, MNRAS, 470, 651
Romeo, A. B., Agertz, O., & Renaud, F. 2023, MNRAS, 518, 1002
Roper, W. J., Lovell, C. C., Vijayan, A. P., et al. 2022, MNRAS, 514, 1921
Scannapieco, C., Wadepuhl, M., Parry, O. H., et al. 2012, MNRAS, 423, 1726
Shankar, F., Marulli, F., Bernardi, M., et al. 2013, MNRAS, 428, 109
Shen, S., Mo, H. J., White, S. D. M., et al. 2003, MNRAS, 343, 978
Shibuya, T., Ouchi, M., & Harikane, Y. 2015, ApJS, 219, 15
Shibuya, T., Ouchi, M., Harikane, Y., et al. 2019, ApJ, 871, 164
Skelton, R. E., Whitaker, K. E., Momcheva, I. G., et al. 2014, ApJS, 214, 24
Snyder, G. F., Lotz, J. M., Rodriguez-Gomez, V., et al. 2017, MNRAS, 468, 207
Speagle, J. S., Steinhardt, C. L., Capak, P. L., et al. 2014, ApJS, 214, 15
Suess, K. A., Kriek, M., Price, S. H., et al. 2019a, ApJ, 877, 103
Suess, K. A., Kriek, M., Price, S. H., et al. 2019b, ApJL, 885, L22
Swinbank, A. M., Harrison, C. M., Trayford, J., et al. 2017, MNRAS, 467, 3140
Szomoru, D., Franx, M., Bouwens, R. J., et al. 2011, ApJL, 735, L22
Szomoru, D., Franx, M., van Dokkum, P. G., et al. 2013, ApJ, 763, 73
Tacchella, S., Carollo, C. M., Förster Schreiber, N. M., et al. 2018, ApJ, 859, 56
Tacchella, S., Carollo, C. M., Renzini, A., et al. 2015, Sci, 348, 314
Tacchella, S., Dekel, A., Carollo, C. M., et al. 2016, MNRAS, 457, 2790
Tacchella, S., Diemer, B., Hernquist, L., et al. 2019, MNRAS, 487, 5416
Tody, D. 1986, Proc. SPIE, 627, 733
Tody, D. 1993, in ASP Conf. Ser. 52, Astronomical Data Analysis Software and Systems II, 52, ed. R. J. Hanisch, R. J. V. Brissenden, & J. Barnes (San Francisco. CA: ASP), 173
Trujillo, I., Förster Schreiber, N. M., Rudnick, G., et al. 2006, ApJ, 650, 18
Tuffs, R. J., Popescu, C. C., Völk, H. J., et al. 2004, A&A, 419, 821
van de Sande, J., Lagos, C. D. P., Welker, C., et al. 2019, MNRAS, 484, 869
van de Ven, G., & van der Wel, A. 2021, ApJ, 914, 45
van der Wel, A., Bell, E. F., Häussler, B., et al. 2012, ApJS, 203, 24
van der Wel, A., Franx, M., van Dokkum, P. G., et al. 2014, ApJ, 788, 28
van der Wel, A., Martorano, M., Häußler, B., et al. 2024, ApJ, 960, 53
van Dokkum, P. G., Leja, J., Nelson, E. J., et al. 2013, ApJL, 771, L35
van Dokkum, P. G., Nelson, E. J., Franx, M., et al. 2015, ApJ, 813, 23
van Dokkum, P. G., Whitaker, K. E., Brammer, G., et al. 2010, ApJ, 709, 1018
Varadaraj, R. G., Bowler, R. A. A., Jarvis, M. J., et al. 2024, MNRAS, 533, 3724
Vincent, R. A., & Ryden, B. S. 2005, ApJ, 623, 137
Vulcani, B., Bamford, S. P., Häußler, B., et al. 2014, MNRAS, 441, 1340
Wang, W., Faber, S. M., Liu, F. S., et al. 2017, MNRAS, 469, 4063
Ward, E., de la Vega, A., Mobasher, B., et al. 2024, ApJ, 962, 176
Whitaker, K. E., Bezanson, R., van Dokkum, P. G., et al. 2017, ApJ, 838, 19
Whitney, A., Conselice, C. J., Bhatawdekar, R., et al. 2019, ApJ, 887, 113
Wickham, H. 2016, ggplot2: Elegant Graphics for Data Analysis (New York: Springer)
Wickham, H., Averick, M., Bryan, J., et al. 2019, JOSS, 4, 1686
Williams, R. J., Quadri, R. F., Franx, M., et al. 2009, ApJ, 691, 1879
Williams, R. J., Quadri, R. F., Franx, M., et al. 2010, ApJ, 713, 738
Wuyts, S., Förster Schreiber, N. M., Nelson, E. J., et al. 2013, ApJ, 779, 135
Yang, L., Roberts-Borsani, G., Treu, T., et al. 2021, MNRAS, 501, 1028